Extreme heat killing more than 100 people in Mexico hotter and much more likely due to climate change

Authors

1. Izidine Pinto, *Royal Netherlands Meteorological Institute (KNMI), De Bilt, The Netherlands;*
2. Clair Barnes, *Grantham Institute – Climate Change and the Environment, Imperial College London, UK*
3. Sjoukje Philip, *Royal Netherlands Meteorological Institute (KNMI), De Bilt, The Netherlands*
4. Sarah Kew, *Royal Netherlands Meteorological Institute (KNMI), De Bilt, The Netherlands*
5. Ruth Cerezo-Mota, *Laboratorio de Ingeniería y Procesos Costeros, Instituto de Ingeniería, Universidad Nacional Autónoma de México, Sisal,Yucatán, México*
6. Arielle Tannenbaum, *Climate Central, Princeton, New Jersey, USA*
7. Shel Winkley, *Climate Central, Princeton, New Jersey, USA*
8. Andrew Pershing, *Climate Central, Princeton, New Jersey, USA*
9. Maja Vahlberg, *Red Cross Red Crescent Climate Centre, the Hague, The Netherlands (based in Ubmeje/Umeå, Sweden)*
10. Carolina Pereira Marghidan, *Red Cross Red Crescent Climate Centre, the Hague, Netherlands, KNMI, De Bilt, Netherlands; University of Twente, Enschede, Netherlands*
11. Karina Izquierdo, *Red Cross Red Crescent Climate Centre, the Hague, Netherlands (based in Mexico City, Mexico)*
12. Sajanika Sivanu, *Red Cross Red Crescent Climate Centre, the Hague, Netherlands (based in Bonn, Germany)*
13. Ladd Keith, *University of Arizona, Tucson, USA; Global Heat Health Information Network (GHHIN)*
14. Michael Kleeman, *University of San Diego, San Diego, USA; American Red Cross, Scientific Advisory Council, USA*
15. Friederike E L Otto, *Grantham Institute – Climate Change and the Environment, Imperial College London, UK*

Review authors
1. Brenda Avila Flores, *Mexican Red Cross, Mexico City, Mexico*
2. Susana Arroyo Barrantes, *International Federation of the Red Cross and Red Crescent Societies (IFRC), Regional Office for the Americas, Panama City, Panama*
3. Roop Singh, *Red Cross Red Crescent Climate Centre, the Hague, Netherlands (based in New Jersey, USA)*
4. Malcolm Mistry, *Red Cross Red Crescent Climate Centre, the Hague, Netherlands; The London School of Hygiene & Tropical Medicine (LSHTM), London, UK*
5. Joyce Kimutai, *Grantham Institute – Climate Change and the Environment, Imperial College London, UK*

Main findings

- The extreme heat in the north and central America has resulted in severe impacts, including more than 125 heat-related deaths in Mexico since March, thousands of cases of heat stroke, and power outages. We likely do not know the full picture of heat-related deaths, since they are usually only confirmed and reported months after the event, if at all.
- Existing drought conditions have further aggravated the situation by preventing the dispersion of polluting particles, decreasing water availability, and reducing hydropower generation and electricity supply.
- Observations show that 5-day maximum temperatures in May-June such as recorded this year are expected to occur about every 15 years in today's climate that has been warmed by 1.2C. However, around the year 2000, when global temperatures were half a degree lower than now, such events were expected to occur only about once every 60 years.
- The night time temperatures over the same 5-day period were also high, but not extreme in today's climate; there is now a 50% chance per year of similar temperatures occurring. At the turn of the millennium such events would only have been expected to occur with a 13% chance in any given year.
- These return times are estimated for the region as a whole. It is important to highlight that the heat was more rare in the southeastern part of the region, especially for the nighttime temperatures with return periods of up to 1000 years in individual locations.
- To determine the role of climate change we combine observations with climate models and we conclude that human-induced warming from burning fossil fuels made the 5-day maximum temperature event about 1.4 degrees hotter and about 35 times more likely. For nighttime temperatures this is about 1.6 degrees hotter and about 200 times more likely.
- These trends will continue with future warming and events like the one observed in 2024 will be very common in a 2C world.
- Extreme heat warning systems and action plans can help fill important gaps in preparedness across Central America. Heat safety protection laws can be enacted and implemented to protect outdoor workers across all countries.
- Strengthened grid resilience and water conservation strategies are critical to ensure reliable services during heat events. Improved urban planning, more green spaces, and enhanced infrastructure in informal settlements will also help protect the most vulnerable.

1 Introduction

Since the end of May and continuing into the first part of June 2024, the Southwest United States, Mexico, and the northern part of Central America have been suffering impacts related to extreme daytime and nighttime heat. National monthly Tmax records have been broken in Mexico (X, X) and Guatemala (X), annual Tmax records have been broken in Honduras (X) and across the southern U.S. (Le Monde), annual average temperature records have been broken in the southwest U.S. (X), and national Tmin records have been broken in Mexico (X).

The southern portion of Mexico, the Yucatan Peninsula, experienced new records of maximum temperature (Tmax), reaching 44.7°C and a heat index of 52.1°C on 17 May (X). The month of May was ranked as the warmest May in historical records (Conagua). While some parts of the country (central and southeast) have since had relief from the scorching temperatures due to the rainy season, the same is not true for the northern part of the country. On 13 June, Mexico reached a Tmax of 51.9°C, the hottest June day ever recorded in the country (X). In the United States of America, the temperature reached 43.9°C in Las Vegas, 44.4°C in Phoenix and 50°C in Death Valley (NWS, 2024) on 6 June.

The 2024 heatwave hit early in the summer season, in a year characterised by a stark contrast from a cooler winter associated with El Niño. The extreme heat hit areas with both high population density and high vulnerability, increasing the impact of the heat. Vulnerabilities and impacts have been exacerbated by forest fires which have ravaged large swathes of land, notably in Honduras, Guatemala, Nicaragua, and El Salvador, exacerbating air pollution levels and prompting health advisories and emergency measures, including banned outdoor activities at schools (Dario Medios, 2024; Climate Central, 2024; E&N, 2024; Gallagher, 2024). In Mexico, existing drought conditions have further aggravated the situation, by preventing the dispersion of polluting particles, as well as decreasing water availability and impacting hydropower generation and electricity supply (Dario Medios, 2024). Moreover, extreme heat increases the risk of dengue, and Latin America and the Caribbean is currently facing its worst outbreak in recorded history with 3.5 million people infected and over 1000 deaths recorded (SwissInfo, 2024). Mexico experienced one of the deadliest heatwaves last year with 421 deaths 10 times more than in 2022 and 47 times more than in 2013, according to official numbers (proceso). This year, the toll so far (up to 12 June) is 125 deaths (SwissInfo) associated with the heatwave and 2,308 affected by heat stroke. Since the beginning of the year, up to today, 5837 forest fires have been registered, covering an extension of almost 619,761.73 ha (CONAGUA). Additionally, there are reports that due to the extreme temperatures, birds (INFOBAE) and hundreds of howler monkeys fell to the ground (National Geographic). Furthermore, this event has shown that the electrical sector might not be prepared to face these extreme temperatures. Several blackouts have been reported during this heatwave (El Financiero). In the United States, extreme heat currently imposes an economic burden of $100 billion annually, a figure projected to rise to $500 billion by 2050 (Mackres et al., 2023). This substantial cost stems from factors including increased healthcare expenses, higher energy demands for cooling, and losses in labour productivity. Notably, Texas alone is responsible for nearly one-third of the national labour productivity losses due to heat stress, highlighting the state's significant vulnerability to extreme heat (Arsht, 2021). In California, annual heat-related emergency visits averaged more than 5,000 between 2010 and 2020, underscoring the heightened vulnerability of populations such as older adults, infants, pregnant individuals, and those with chronic conditions (California Air Resources Board, 2024). In 2023, heat-related deaths in

the Phoenix, Arizona region increased by 52% compared to the previous year with the most heat related deaths ever recorded (Maricopa County, 2024). In Monterrey, Mexico, heat and humidity are estimated to lead to $1.8 billion of economic loss due to reduced annual labour productivity, projected to double by 2050 (Arsht-Rock, n.d.). Furthermore, the recent Lancet report on Latin America, covering El Salvador, Guatemala, and Honduras, states that heat-related deaths and risks for outdoor workers across the region have increased significantly (Hartinger et al., 2024). For example, Honduras saw a 204% increase in estimated annual average number of heat-related fatalities from the 2000-2009 to 2013-2022.

The area experiencing intense heat is under the influence of a large and lingering region of high pressure or anticyclonic circulation (Figure 1), known as a 'heat dome' (AMS). A jet stream anomaly facilitated the eastward transport of very warm air across Mexico. The rising warm surface air within a heat dome is effectively trapped under subsiding air from above and continues to warm from incoming sunshine, with clearer than normal skies. The associated subsidence in this case led to the driest spring on record for Mexico. Excessive heat combined with antecedent dryness, worsens drought conditions. Heat and drought are commonly linked in a feedback loop – heat exacerbates drought, which, in turn, worsens heat. During this period hot temperatures were experienced across Central America and the United States, including Texas and Florida. Warmer-than-average sea-surface temperatures in the eastern Pacific and Gulf of Mexico increased humidity levels, exacerbating discomfort in addition to the already excessive temperatures. In a recent study (Zhang et al., 2023), it was found that this type of atmospheric circulation over the region is projected to increase and, with this, an increase in heat events and affected population.
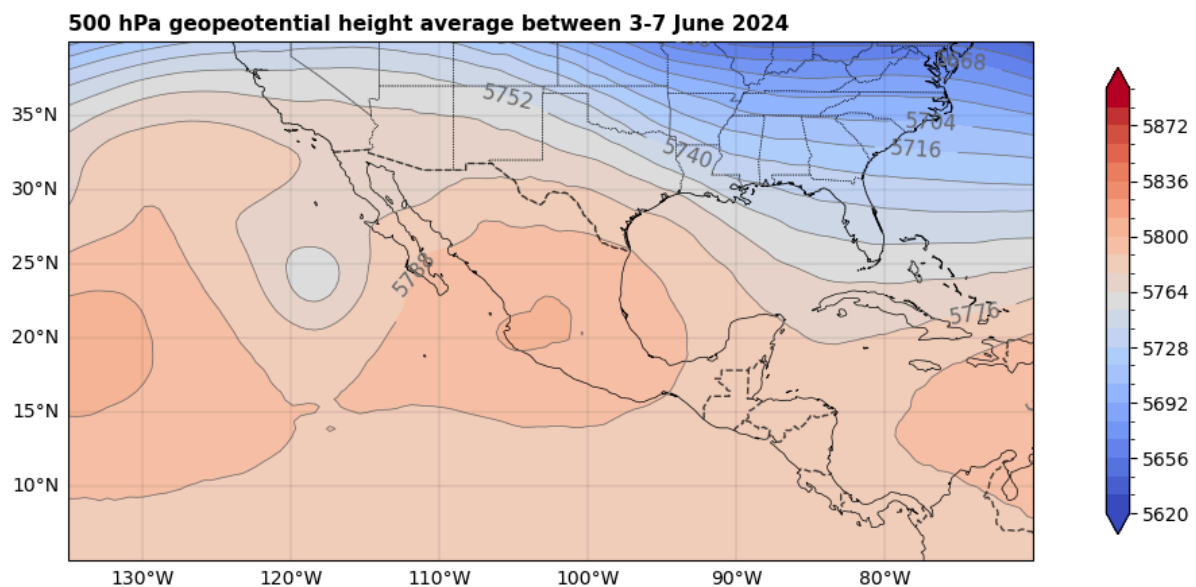

Figure 1. Average 500 hPa geopotential height (m) during 3-7 June 2024 indicating that there was a heat dome of higher pressure this time of year over Mexico. Source: ERA5.

1.1 Events in the region

Extremely high maximum and minimum temperatures have increased globally since 1950 and across most land areas, including Central America. In North America, minimum temperatures have increased

consistently across the region, while maximum temperatures show smaller or no trends in some parts of the region (Seneviratne et al., 2021). Observations reveal a clear increase in the intensity and frequency of hot days over these regions (Dunn et al., 2020) while heatwave length and intensity have increased less than in most other land areas of the world Perkins-Kirkpatrick and Lewis, 2020). In an attribution study on heat extremes globally, Easterling et al. (2016) found a strong trend attributable to human-induced climate change over Mexico. In an attribution study over Mexico and the U.S. looking not only at greenhouse gases but also aerosol forcings and internal variability, Gracia-Martinez and Bollasina (2021) found that anthropogenic greenhouse gases increased the likelihood of heatwaves using three different heatwave indicators, but that aerosol-induced cooling, in particular between 1950 and 1980, masked these trends and in some places even led to small cooling trends. The ENSO has also been observed to increase the intensity (Luo and Lau) and the frequency (Murari, et al 2016) of heatwaves. This region stands out as a global hotspot, both in observations and projections, with stronger trends in absolute summer maximum temperatures in northern Mexico and the southern U.S. and stronger trends in nighttime temperatures in southern Mexico and Central America (Suarez-Gutierrez et al. 2020).

1.2 Event Definition

Based on the impacts and record temperatures described in the sections above, we defined the area as a large region encompassing Mexico and neighbouring states (figure 2). In the north this region includes Texas, most of New Mexico and Arizona, and it extends to the west coast such that Las Vegas is within the study area. In the south, the region includes Belize, Guatemala, Honduras, and El Salvador. We analyse the hottest 5-day temperatures in the months May and June, Tx5x. To also include impacts related to nighttime heat, we additionally study the hottest 5-night temperatures in May-June, Tn5x.

Figure 3 shows the seasonal cycle of maximum and minimum temperature over the study area, as shown in figure 2. Each grey line represents all previous years in the data set, and the red line shows the current year. It is apparent that the seasonal peak occurs usually somewhere between June and August. However, this year has been unusual with a peak early in the season. Extreme temperatures that occur early in the season are known to be more impactful than in mid-season because people are not prepared for the heat. We therefore focus on the months May and June rather than an annual maximum averaged over the whole study area. Averaged over the study region, the hottest 5-day period occurred over 3-7 June and the hottest 5-night period occurred over 5-9 June (figure 2).
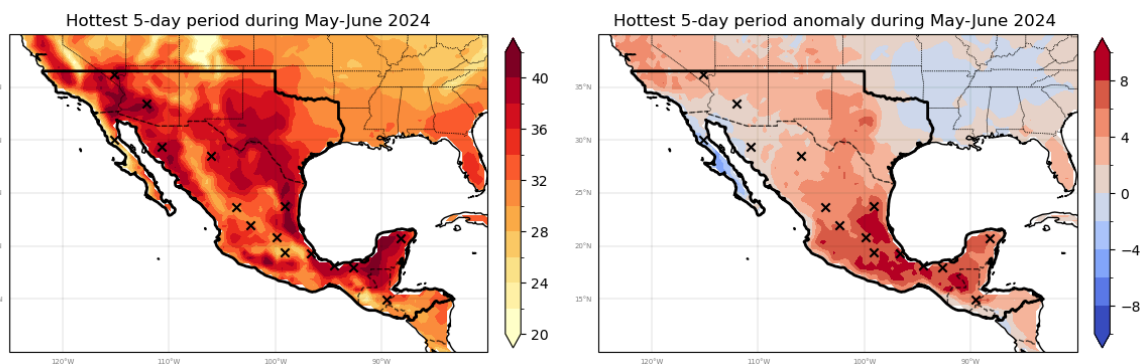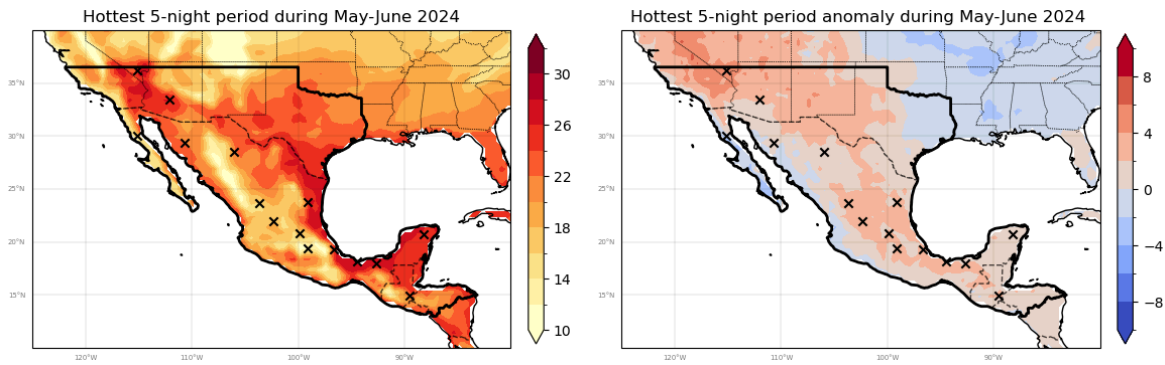
Figure 2. Hottest 5-day period for maximum daytime temperatures (Tx5x) and anomaly (top) and maximum nighttime temperatures (Tn5x) and anomaly (bottom). The thick black contour shows the study region. Black crosses show the locations where impacts or temperature records have been reported. Source: ERA5 data.
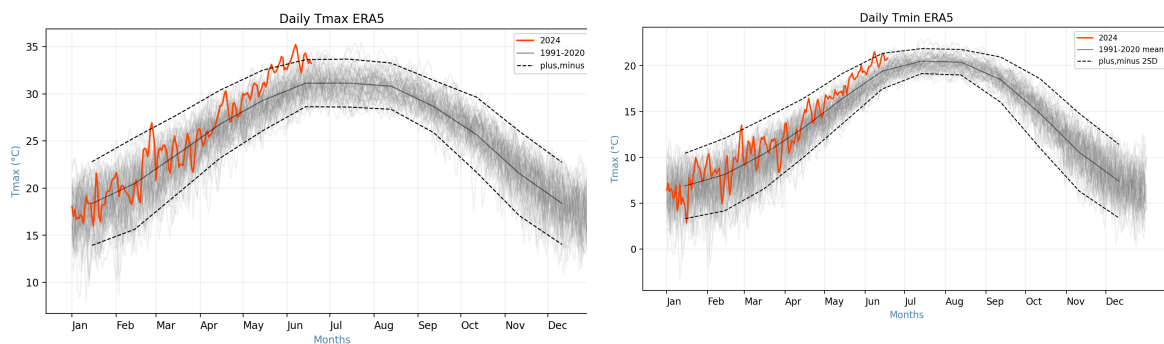

Figure 3. Daily variability of maximum (left) and minimum (right) temperature over the study area from ERA5 data. Red line shows the current year temperature evolution compared with all previous years (in grey). Solid black line shows the climatology and dotted line shows two standard deviations from the mean for the period 1991-2020.

2 Data and methods

2.1 Observational data

Three gridded observational datasets are used.

1. The European Centre for Medium-Range Weather Forecasts's 5th generation reanalysis product, ERA5, is a gridded dataset that combines historical observations into global estimates using advanced modelling and data assimilation systems (Hersbach et al., 2020). We analyse maximum and minimum daily 2m temperature from this product. This data was downloaded from KNMI Climate Explorer at 0.5° × 0.5° for the years 1950 to present.

2. MSWX (Multi-Source Weather) dataset (Beck et al., 2022), which combines various observational and reanalysis-based data for reliable bias-corrected weather variable estimates, at 3-hourly intervals

from 1979 to near real-time, and at 0.1° spatial resolution globally. We use daily minimum and maximum temperature from this product.

3. The CPC Global Unified Daily Gridded dataset. This is the gridded product from NOAA PSL, Boulder, Colorado, USA, available at 0.5° x 0.5° resolution, for the period 1979-present. Data are available from NOAA. We use CPC daily minimum and maximum temperature.

As a measure of anthropogenic climate change, we use the (4-year low-pass filtered) global mean surface temperature (GMST), where GMST is taken from the National Aeronautics and Space Administration (NASA) Goddard Institute for Space Science (GISS) surface temperature analysis (GISTEMP, Hansen et al., 2010 and Lenssen et al. 2019).

2.2 Model and experiment descriptions

We use two multi-model ensembles from climate modelling experiments using different framings (Philip et al., 2020): Regional climate models and coupled global circulation models.

1. Coupled Model Intercomparison Project Phase 6 (CMIP6), which consists of simulations from 20 participating models with varying resolutions. For more details on CMIP6, please see Eyring et al., (2016). For all simulations, the period 1850 to 2015 is based on historical simulations, while the SSP5-8.5 scenario is used for the remainder of the 21st century.

2. Coordinated Regional Climate Downscaling Experiment CORDEX-CORE (13 models at 0.44° resolution (SAM-44) and 9 models at 0.22° resolution (SAM-22)) multi-model ensemble (Giorgi and Gutowski, 2015; Giorgi et al., 2021), comprising 14 simulations resulting from pairings of Global Climate Models (GCMs) and Regional Climate Models (RCMs)). These simulations are composed of historical simulations up to 2005, and extended to the year 2100 using the RCP8.5 scenario.

3. HighResMIP SST-forced model ensemble (Haarsma et al. 2016), the simulations for which span from 1950 to 2050. The SST and sea ice forcings for the period 1950-2014 are obtained from the 0.25° x 0.25° Hadley Centre Global Sea Ice and Sea Surface Temperature dataset that have undergone area-weighted regridding to match the climate model resolution (see Table B). For the 'future' time period (2015-2050), SST/sea-ice data are derived from RCP8.5 (CMIP5) data and combined with greenhouse gas forcings from SSP5-8.5 (CMIP6) simulations (see Section 3.3 of Haarsma et al. 2016 for further details).

2.3 Statistical methods

Methods for observational and model analysis and for model evaluation and synthesis are used according to the World Weather Attribution Protocol, described in Philip et al., (2020), with supporting details found in van Oldenborgh et al., (2021), Ciavarella et al., (2021) and WWA, 2021. The key steps, presented in sections 3-6, are: (3) trend estimation from observations; (4) model evaluation; (5) multi-method multi-model attribution; and (6) synthesis of the attribution statement.

In this report we analyse time series of five-day maximum of maximum temperature (Tx5x) and five-day maximum of minimum temperature (Tn5x)

A nonstationary normal distribution is used to model both Tx5x and Tn5x. The distribution is assumed to shift linearly with the covariates, while the variance remains constant. The parameters of the statistical model are estimated using maximum likelihood.

For each time series we calculate the return periods, probability ratio (PR; the factor-change in the event's probability) and change in intensity of the event under study for the 2024 GMST and for 1.2 C cooler GMST: this allows us to compare the climate of now and of the preindustrial past (1850-1900, based on the Global Warming Index).

3 Observational analysis: return period and trend

3.1 Analysis of point station data and gridded data

Figure 4 shows the May-June maximum of Tmax (Tx5x) over the study region shown in Figure 2 for the three gridded observational datasets. These values have been evaluated against a few stations with long time series but often no recent data that are available via the GHCN-D station dataset (not shown), accessed via the KNMI Climate Explorer. Aside from quite a large offset in most cases, there's no evidence that the gridded datasets are misrepresenting the trend or variability. Even in recent years there's not clear evidence of a trend in most of the selected stations, and in some instances (stations El Tule, Pabellon), there has been a cluster of warmer years in the 1950s, as also seen in ERA5. Therefore we use all three gridded datasets.

The 2024 Tx5x values were extremely high, although, except for CPC, not the record hottest. We analyse the area average Tx5x for all three gridded datasets and calculate the return period, change in intensity and probability ratio (along with the 95% confidence interval) between the current climate of 2024 and a past climate that is 1.2℃ cooler by fitting the data to a Generalised Extreme Value (GEV) distribution. Figure 5 shows the annual maxima time series and the fits to the normal distribution. The return period and magnitude are listed in Table 3.1. While ERA5 and CPC show approximately the same return period, MSWX is an outlier with a slightly lower return period. Based on the three datasets, we use a return period of 15 years for the model analysis. Best estimates of the probability ratios (see Table 5.1) range from 13 (ERA5) to 69 (MSWX). For the intensity change, this ranges from 1.4℃ (ERA5) to 2.2℃ (MSWX). As the study area is quite large, we additionally spatially analyse return periods and trends across the region. In the spatial analysis (Figure 6), the return period, change in intensity, and probability ratio are higher over Mexico, indicating that this event has been more unusual there compared to parts of the USA.

The 2024 Tn5x values were less extreme, except in CPC, see Figure 7. We again analyse the area average Tx5x for all three gridded datasets and calculate the return period, change in intensity and probability ratio (along with the 95% confidence interval) between the current climate of 2024 and a past climate that is 1.2℃ cooler by fitting the data to a normal distribution. Figure 8 shows the annual maxima time series and the fits to the normal distribution. The return period and magnitude are listed in Table 3.1. While ERA5 and CPC again show approximately the same return period, MSWX is very much an outlier with a very high return period. Therefore we base the return period we use for the

model analysis on ERA5 and CPC only, we use a return period of 2 years. Best estimates of the probability ratios (see Table 5.2) range from 36 (ERA5) to infinity (MSWX), which is not unexpected given the high magnitude of the 2024 event in this dataset. For the intensity change this ranges from 1.4℃ (ERA5) to 3.5℃ (MSWX). For the spatial analysis (Figure 9), similarly to Tx5x, this event has been more unusual in Mexico, Guatemala, Honduras and El Salvador.

Additionally, we analysed trends and intensity changes between the current climate and the climate of around the year 2000, which is about 0.5℃ cooler than the current climate of 2024. From this analysis we conclude that where the Tx5x event in today's climate is a 1-in-15 year event, this would have been a 1-in-60 year event around 2000. Such an event would have been 0.8℃ cooler than now. For Tn5x we find that where this is a 1-in-2 year event in today's climate, it would have been a 1-in-8-year event around 2000. Such an event would have been 0.8℃ cooler than now.

Table 3.1: Estimated return periods of Tx5x and Tn5x events over the study region.

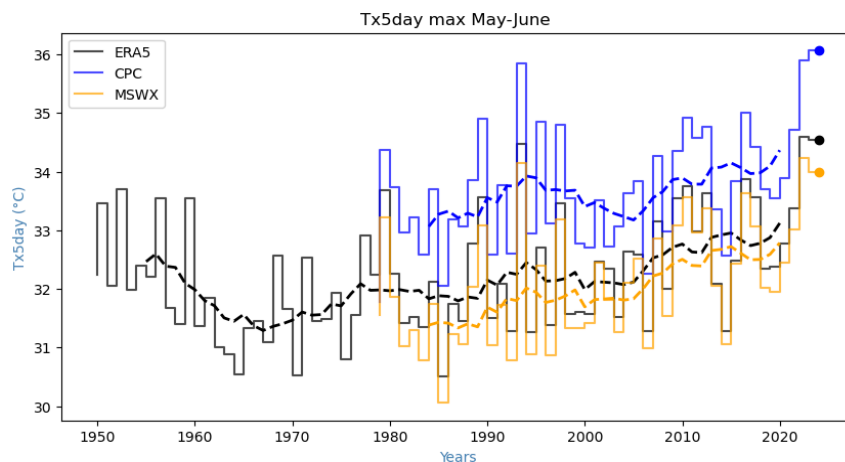| Dataset	Tx5x		Tn5x	
	Magnitude (℃)	Return period (95% C.I.)	Magnitude (℃)	Return period (95% C.I.)
ERA5	34.5	16	20.8	1.8
CPC	36	19	21.2	1.6
MSWX	33.9	7	21.6	180

Figure 4. May-June maximum of Tmax (Tx5x) over the study region shown in Figure 1. The dotted red line represents the 10 year moving average. The dot shows the event in June 2024.
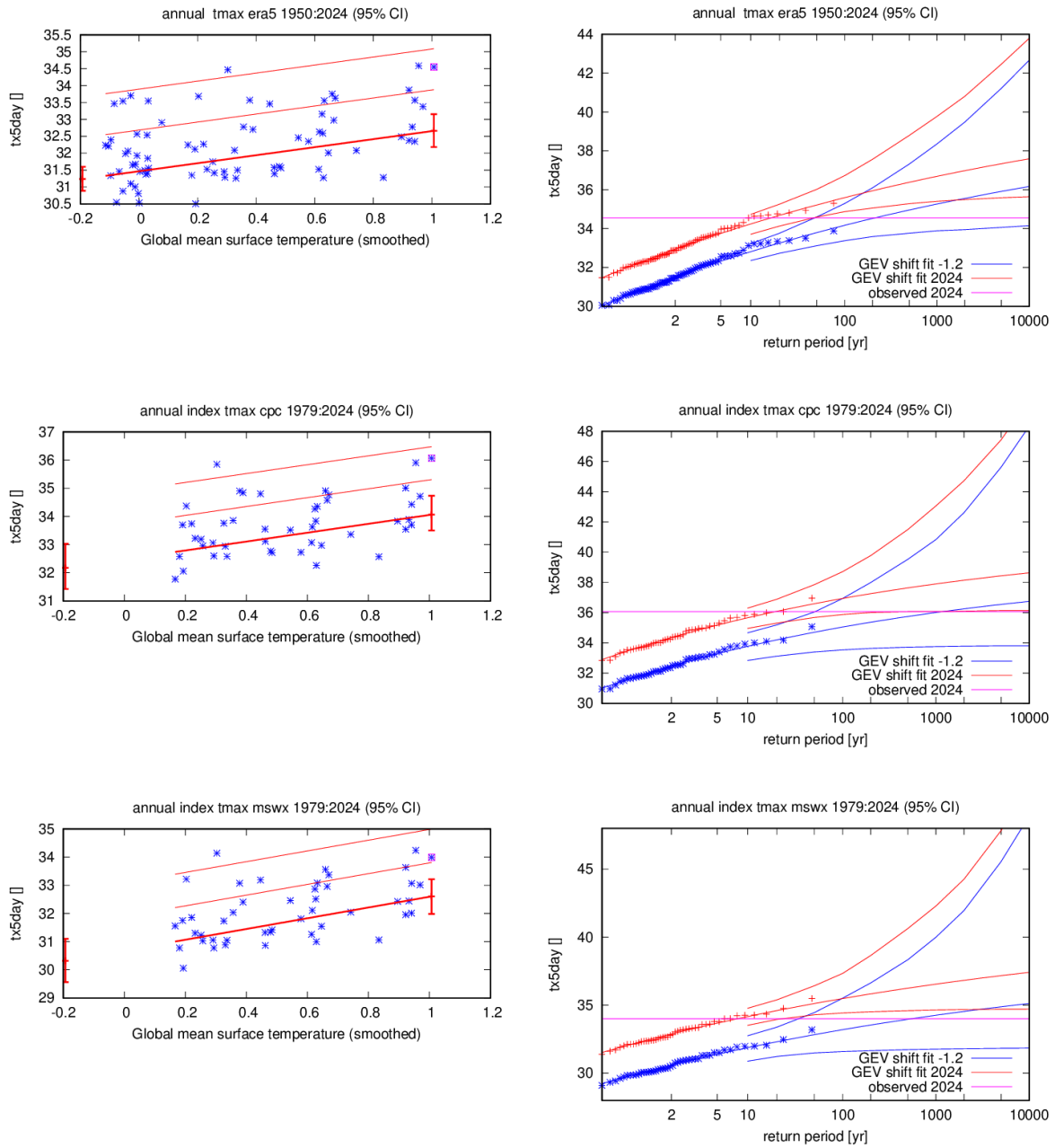
Figure 5. Tx5x over the study region estimated from ERA5 (top), CPC (middle) and MSWX (bottom) records shown against the change in global mean temperature. The thick red line denotes the time-varying mean. The vertical red lines show the 95% confidence interval for the location parameter, for the current, 2024 climate and the 1.2℃ cooler climate. The 2024 observation is highlighted with the pink box (left). Return periods for the 2024 climate (red lines) and the 1.2℃ cooler climate (blue lines with 95% CI) (right).
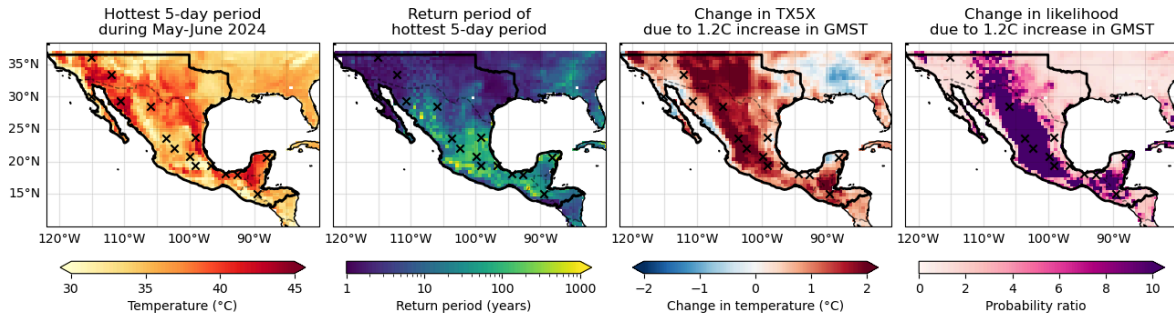
Figure 6. Tx5x Event magnitude, best estimates of return period, change in intensity and probability ratios. Black crosses show the locations where impacts or temperature records have been reported. Data ERA5.
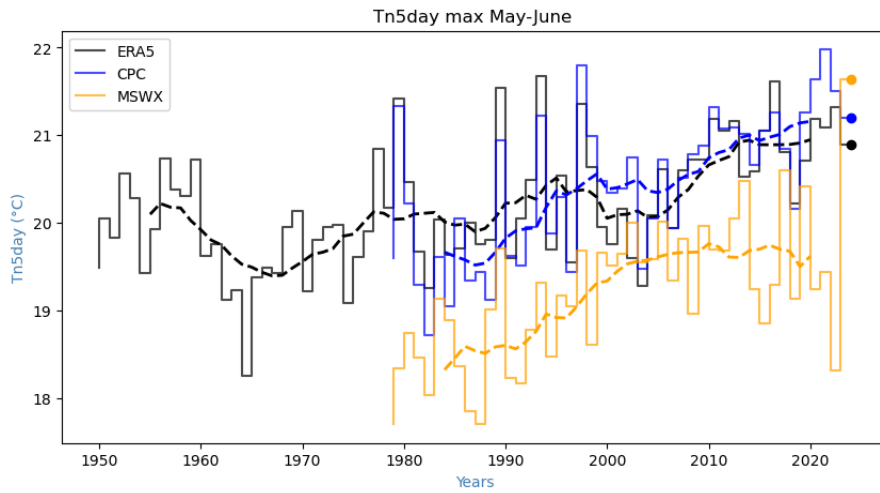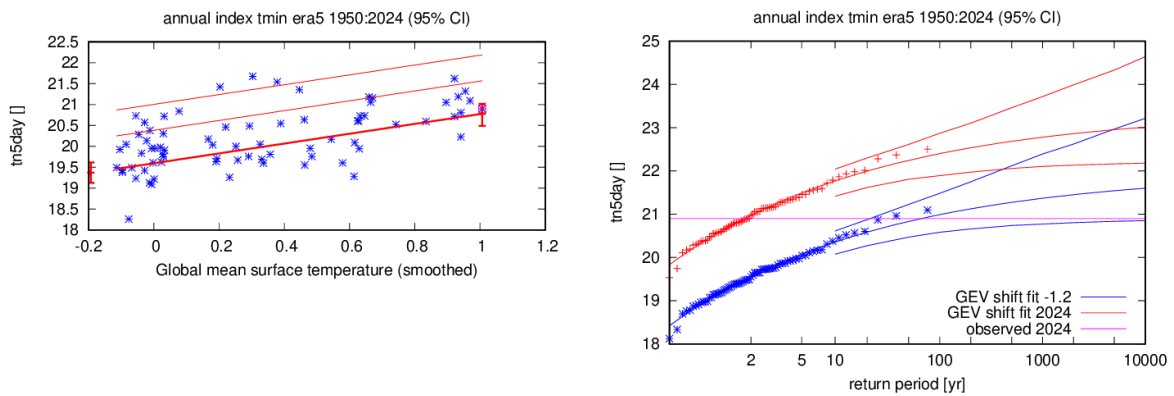

Figure 7. May-June maximum of Tmax (Tx5x) over the study region shown in Figure 1. The dotted red line represents the 10 year moving average. The dot shows the event in June 2024.
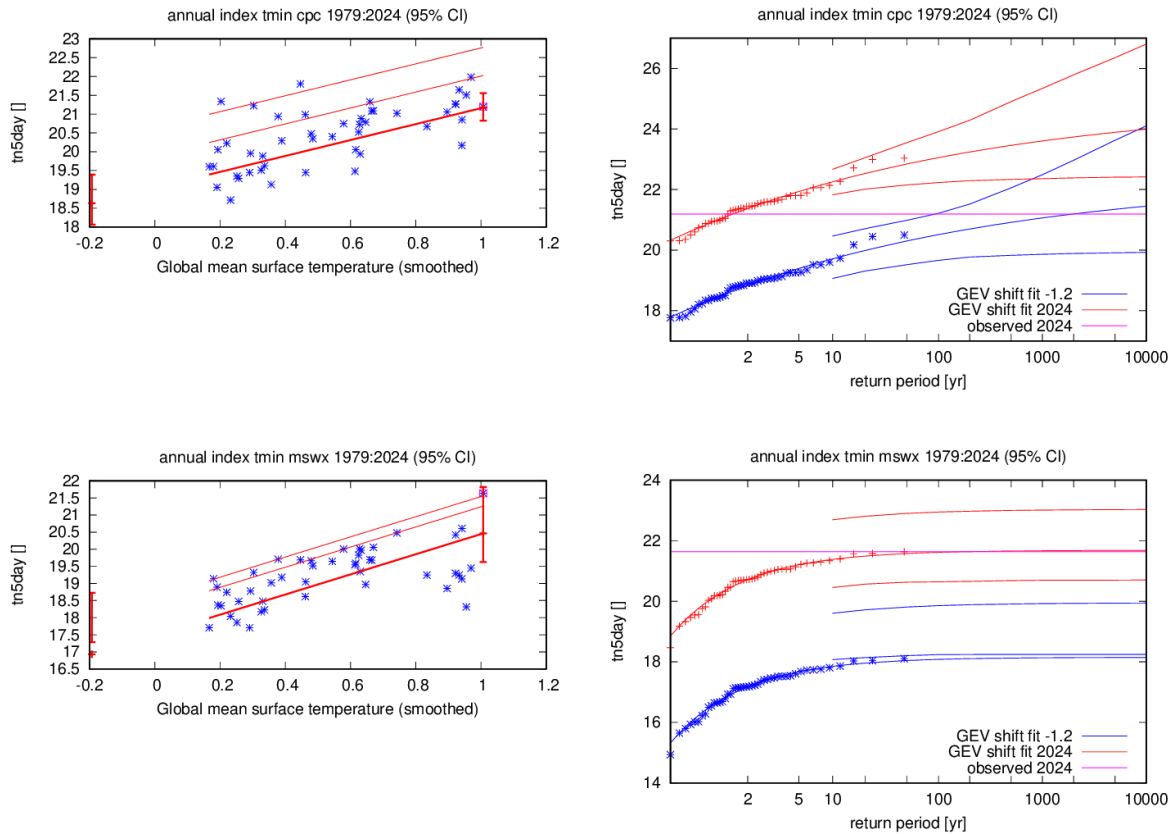
Figure 8. Tn5x over the study region estimated from ERA5 (top), CPC (middle) and MSWX (bottom) records shown against the change in global mean temperature. The thick red line denotes the time-varying mean. The vertical red lines show the 95% confidence interval for the location parameter, for the current, 2024 climate and the 1.2℃ cooler climate. The 2024 observation is highlighted with the pink box (left). Return periods for the 2024 climate (red lines) and the 1.2℃ cooler climate (blue lines with 95% CI) (right).
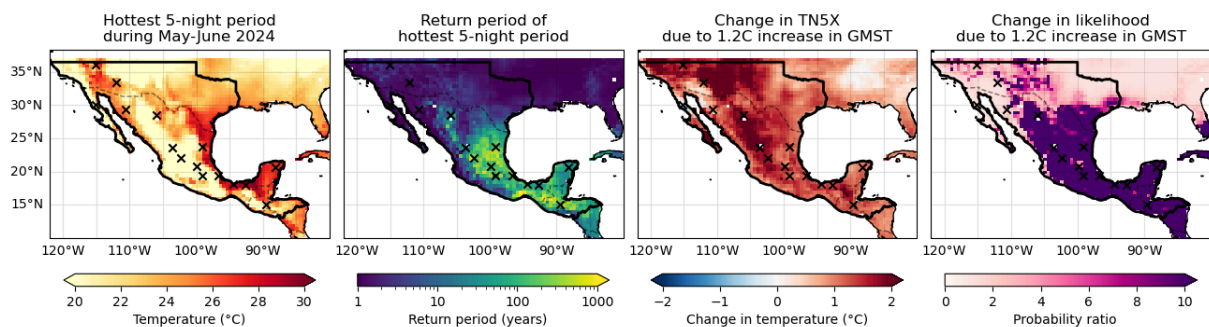

Figure 9. Tx5x Event magnitude, best estimates of return period, change in intensity and probability ratios. Black crosses show the locations where impacts or temperature records have been reported. Data ERA5.

4 Model evaluation

In this section, we show the results of the model evaluation for the Tx5x and Tn5x events averaged over the study region. Per framing or model setup, we also use models that only pass the evaluation

tests if we only have five models or less for that framing that perform well. This means we use only the models labelled 'good' for the CMIP6, CORDEX and HighResMIP ensemble.

Tables 4.1 and 4.2 show the model evaluation results for Tx5x and Tn5x, respectively. The climate models are evaluated against the observations in their ability to capture:

1. Spatial patterns: Models that do not match the observations in terms of the spatial patterns are excluded (Figures A1,A3,A5,A7,A9,A11).

2. Seasonal cycles: For this, we qualitatively compare the model outputs against observations-based plots. We discard the models that exhibit multi-modality and/or ill-defined peaks in their seasonal cycles. We also discard the model if temperature seasonality varies significantly from the observations (Figures A2,A4,A6,A8,A10,A12).

3. Parameters of the fitted GEV model. We discard the model if the model and observation parameters ranges do not overlap (Tables 1).

Table 4.1. Evaluation results of the climate models considered for attribution analysis of Tx5x over the study region. For each model, the expected temperature of a 1-in-15-year event is shown, along with the best estimate of the Sigma and Shape parameters and a 95% confidence interval for each, obtained via bootstrapping. The qualitative evaluation is shown in the right-hand column. Based on overall suitability, the models are classified as good, reasonable or bad, shown by green, yellow and red highlights, respectively.

Model / Observations	Threshold for return period 15 yr (˚C)	Seasonal cycle	Spatial pattern	Sigma	Shape parameter	Conclusion
ERA5	34.5			0.760 (0.590 ... 0.910)	-0.080 (-0.27 ... 0.13)	
CPC	36			0.800 (0.570 ... 1.02)	-0.11 (-0.54 ... 0.21)	
MSWX	33.9			0.760 (0.530 ... 0.940)	-0.080 (-0.45 ... 0.24)	
CMIP6:						
ACCESS-CM2	35.04	good	good	1.01 (0.750 ... 1.16)	-0.20 (-0.58 ... -0.030)	good
ACCESS-ESM1-5	36.13	good	good	0.900 (0.660 ... 1.10)	0.050 (-0.22 ... 0.23)	good
CanESM5	36.98	good	good	0.740 (0.570 ... 0.870)	-0.19 (-0.38 ... -0.050)	good
CMCC-ESM2	33.9	good	good	0.980 (0.760 ... 1.13)	-0.18 (-0.34 ... 0.0)	good
CNRM-CM6-1-HR	32.51	reasonable	good	1.06 (0.800 ... 1.22)	-0.28 (-0.46 ... -0.12)	reasonable
CNRM-CM6-1	33.1	reasonable	good	0.900 (0.680 ... 1.05)	-0.040 (-0.43 ... 0.13)	reasonable
EC-Earth3	35.05	good	good	0.960 (0.780 ... 1.07)	-0.25 (-0.46 ... -0.070)	good
EC-Earth3-Veg	34.8	good	good	0.850 (0.600 ... 1.02)	-0.10 (-0.42 ... 0.080)	good
EC-Earth3-Veg-LR	34.21	good	good	0.990 (0.710 ... 1.15)	-0.22 (-0.38 ... 0.010)	good
FGOALS-g3	33.86	good	good	0.760 (0.580 ... 0.890)	-0.070 (-0.26 ... 0.10)	good
INM-CM4-8	37.04	reasonable	good	1.23 (0.980 ... 1.38)	-0.19 (-0.37 ... -0.010)	reasonable
INM-CM5-0	37.63	good	good	1.41 (1.12 ... 1.63)	-0.17 (-0.45 ... 0.020)	bad
IPSL-CM6A-LR	31.53	reasonable	good	1.00 (0.730 ... 1.17)	-0.23 (-0.40 ... -0.060)	reasonable
MIROC6	46.43	bad	bad	1.25 (0.830 ... 1.45)	-0.18 (-0.39 ... 0.17)	bad
MPI-ESM1-2-HR	36.09	good	good	0.850 (0.640 ... 1.02)	-0.070 (-0.27 ... 0.080)	good
MPI-ESM1-2-LR	34.42	good	good	0.950 (0.730 ... 1.08)	-0.20 (-0.54 ... 0.0)	good

Model / Observations	Threshold for return period 15 yr (˚C)	Seasonal cycle	Spatial pattern	Sigma	Shape parameter	Conclusion
MRI-ESM2-0	35.27	good	good	0.960 (0.750 ... 1.09)	-0.18 (-0.44 ... 0.060)	good
NorESM2-LM	36.28	good	bad	0.760 (0.550 ... 0.920)	-0.040 (-0.32 ... 0.15)	bad
NorESM2-MM	35.09	good	good	0.900 (0.680 ... 1.04)	-0.25 (-0.45 ... -0.070)	good
TaiESM1	35.46	good	good	1.06 (0.780 ... 1.22)	-0.14 (-0.32 ... 0.040)	reasonable
CORDEX:						
CAM-22_CCCma-CanESM2_CRCM5	34.642	reasonable	bad	0.800 (0.626 ... 0.932)	-0.13 (-0.41 ... 0.057)	bad
CAM-22_CNRM-CERFACS-CNRM-CM5_CRCM5	32.094	good	bad	1.18 (0.841 ... 1.42)	-0.64 (-0.88 ... -0.21)	bad
CAM-22_MOHC-HadGEM2-ES_RegCM4-7	35.187	good	good	0.762 (0.572 ... 0.923)	-0.18 (-0.46 ... -0.0010)	good
CAM-22_MOHC-HadGEM2-ES_REMO2015	36.975	good	bad	0.905 (0.693 ... 1.06)	-0.20 (-0.42 ... -0.011)	bad
CAM-22_MPI-M-MPI-ESM-LR_REMO2015	35.845	good	bad	0.849 (0.610 ... 1.00)	-0.12 (-0.33 ... 0.12)	bad
CAM-22_MPI-M-MPI-ESM-MR_RegCM4-7	35.638	good	good	0.686 (0.459 ... 0.909)	-0.038 (-0.42 ... 0.45)	good
CAM-22_NCC-NorESM1-M_REMO2015	36.143	good	bad	0.744 (0.582 ... 0.890)	-0.40 (-0.70 ... -0.24)	bad
CAM-22_NOAA-GFDL-GFDL-ESM2M_CRCM5	32.098	good	bad	0.839 (0.593 ... 1.02)	-0.41 (-0.71 ... -0.15)	bad
CAM-22_NOAA-GFDL-GFDL-ESM2M_RegCM4-7	34.074	good	good	1.01 (0.693 ... 1.25)	-0.082 (-0.39 ... 0.37)	good
CAM-44_CCCma-CanESM2_CRCM5	34.625	reasonable	bad	0.891 (0.603 ... 1.09)	-0.21 (-0.49 ... 0.020)	bad
CAM-44_CCCma-CanESM2_RCA4	35.083	reasonable	reasonable	0.835 (0.607 ... 1.05)	-0.29 (-0.60 ... -0.041)	reasonable
CAM-44_CNRM-CERFACS-CNRM-CM5_RCA4	32.778	reasonable	reasonable	1.23 (0.941 ... 1.47)	-0.41 (-0.74 ... -0.16)	reasonable
CAM-44_CSIRO-QCCCE-CSIRO-Mk3-6-0_RCA4	35.054	reasonable	reasonable	0.871 (0.665 ... 1.10)	-0.10 (-0.55 ... 0.17)	reasonable
CAM-44_ICHEC-EC-EARTH_RCA4	32.769	good	reasonable	0.916 (0.678 ... 1.10)	-0.28 (-0.55 ... -0.0036)	reasonable
CAM-44_IPSL-IPSL-CM5A-MR_RCA4	34.901	reasonable	reasonable	0.860 (0.567 ... 1.08)	-0.15 (-0.56 ... 0.25)	reasonable
CAM-44_MIROC-MIROC5_RCA4	33.784	good	reasonable	1.10 (0.824 ... 1.32)	-0.27 (-0.61 ... 0.0036)	reasonable
CAM-44_MOHC-HadGEM2-ES_RCA4	34.558	good	reasonable	0.948 (0.661 ... 1.21)	-0.093 (-0.36 ... 0.29)	reasonable
CAM-44_MOHC-HadGEM2-ES_RegCM4-3	32.759	good	good	0.634 (0.408 ... 0.850)	-0.0044 (-0.41 ... 0.47)	good
CAM-44_MPI-M-MPI-ESM-LR_RCA4	33.865	good	reasonable	1.14 (0.841 ... 1.40)	-0.12 (-0.62 ... 0.18)	reasonable
CAM-44_MPI-M-MPI-ESM-MR_RegCM4-3	32.288	good	good	0.704 (0.524 ... 0.831)	-0.24 (-0.51 ... -0.055)	good
CAM-44_NCC-NorESM1-M_RCA4	33.365	good	reasonable	0.945 (0.690 ... 1.31)	-0.25 (-0.85 ... 0.032)	reasonable
CAM-44_NOAA-GFDL-GFDL-ESM2M_RCA4	31.873	reasonable	reasonable	0.855 (0.674 ... 1.01)	-0.25 (-0.62 ... -0.060)	reasonable
HighResMIP:						
EC-Earth3P-HR	36.131	good	good	0.798 (0.575 ... 1.02)	-0.22 (-0.59 ... 0.010)	good
EC-Earth3P	36.711	good	good	0.975 (0.716 ... 1.21)	-0.27 (-0.61 ... -0.023)	good
HadGEM3-GC31-HM	37.333	good	good	1.02 (0.726 ... 1.28)	-0.27 (-0.57 ... 0.044)	reasonable
HadGEM3-GC31-LM	37.331	good	good	0.837 (0.597 ... 1.01)	-0.13 (-0.45 ... 0.11)	good
HadGEM3-GC31-MM	36.667	good	good	1.12 (0.824 ... 1.34)	-0.34 (-0.66 ... -0.056)	reasonable
MPI-ESM1-2-HR	36.809	good	good	1.15 (0.730 ... 1.45)	-0.38 (-0.72 ... -0.094)	reasonable
MPI-ESM1-2-XR	36.602	good	good	0.930 (0.557 ... 1.22)	-0.50 (-0.84 ... -0.12)	good

Table 4.2. Evaluation results of the climate models considered for attribution analysis of Tn5x over the study region. For each model, the expected temperature of a 1-in-15-year event is shown, along with the best estimate of the Sigma and Shape parameters and a 95% confidence interval for each, obtained via bootstrapping. The qualitative evaluation is shown in the right-hand column. Based on overall suitability, the models are classified as good, reasonable or bad, shown by green, yellow and red highlights, respectively.

Model / Observations	Threshold for return period 2 yr	Seasonal cycle	Spatial pattern	Sigma	Shape parameter	Conclusion
ERA5	20.8			**0.550 (0.410 ... 0.650)**	**-0.21 (-0.35 ... -0.010)**	
CPC	21.2			0.560 (0.420 ... 0.670)	-0.15 (-0.42 ... 0.030)	
MSWX	21.6			0.760 (0.540 ... 0.880)	-0.62 (-1.1 ... -0.41)	
CMIP6						
ACCESS-CM2	21.24	good	good	0.490 (0.340 ... 0.570)	-0.23 (-0.40 ... 0.040)	good
ACCESS-ESM1-5	21.88	good	good	0.460 (0.350 ... 0.550)	-0.030 (-0.22 ... 0.15)	good
CanESM5	23.2	good	good	0.490 (0.350 ... 0.570)	-0.23 (-0.47 ... 0.010)	good
CMCC-ESM2	21.63	good	good	0.430 (0.340 ... 0.500)	-0.080 (-0.27 ... 0.090)	good
CNRM-CM6-1-HR	17.38	reasonable	bad	0.660 (0.480 ... 0.790)	-0.25 (-0.40 ... -0.070)	bad
CNRM-CM6-1	18.03	reasonable	bad	0.490 (0.360 ... 0.580)	0.0 (-0.18 ... 0.21)	bad
EC-Earth3	20.56	good	good	0.620 (0.450 ... 0.720)	-0.32 (-0.57...-0.07)	good
EC-Earth3-Veg	20.46	good	good	0.580 (0.440 ... 0.670)	-0.13 (-0.56 ... 0.0)	good
EC-Earth3-Veg-LR	19.58	good	good	0.600 (0.420 ... 0.720)	-0.15 (-0.33 ... 0.080)	good
FGOALS-g3	20.18	good	good	0.630 (0.440 ... 0.730)	-0.23 (-0.44 ... 0.010)	good
INM-CM4-8	20.99	good	good	0.440 (0.330 ... 0.500)	-0.23 (-0.37 ... -0.070)	good
INM-CM5-0	20.78	good	good	0.500 (0.330 ... 0.600)	-0.35 (-0.55 ... -0.12)	good
IPSL-CM6A-LR	19.7	good	good	0.390 (0.260 ... 0.490)	0.020 (-0.18 ... 0.22)	reasonable
MIROC6	26.06	reasonable	bad	0.550 (0.400 ... 0.660)	-0.14 (-0.35 ... 0.040)	bad
MPI-ESM1-2-HR	22.97	good	good	0.670 (0.510 ... 0.770)	-0.28 (-0.50 ... -0.12)	good
MPI-ESM1-2-LR	21.71	good	good	0.720 (0.470 ... 0.840)	-0.24 (-0.42 ... 0.030)	good
MRI-ESM2-0	21.46	good	good	0.650 (0.470 ... 0.750)	-0.18 (-0.40 ... 0.080)	good
NorESM2-LM	23.98	reasonable	good	0.480 (0.340 ... 0.570)	-0.080 (-0.30 ... 0.080)	reasonable
NorESM2-MM	22.71	good	good	0.510 (0.380 ... 0.610)	-0.060 (-0.28 ... 0.14)	good
CORDEX:						
CAM-22_CCCma-CanESM2_CRCM5	19.62	good	bad	0.428 (0.292 ... 0.509)	-0.11 (-0.39 ... 0.15)	bad

Model / Observations	Threshold for return period 2 yr	Seasonal cycle	Spatial pattern	Sigma	Shape parameter	Conclusion
CAM-22_MOHC-HadGEM2-ES_RegCM4-7	22.36	good	good	0.594 (0.440 ... 0.725)	-0.26 (-0.53 ... -0.085)	good
CAM-22_MOHC-HadGEM2-ES_REMO2015	22.06	good	bad	0.442 (0.336 ... 0.518)	-0.35 (-0.72 ... -0.010)	bad
CAM-22_MPI-M-MPI-ESM-LR_REMO2015	21.78	good	bad	0.515 (0.368 ... 0.681)	-0.25 (-0.70 ... 0.022)	bad
CAM-22_MPI-M-MPI-ESM-MR_RegCM4-7	21.84	good	good	0.607 (0.440 ... 0.737)	-0.29 (-0.70 ... -0.080)	good
CAM-22_NOAA-GFDL-GFDL-ESM2M_CRCM5	17.28	good	good	0.434 (0.313 ... 0.532)	-0.29 (-0.55 ... -0.11)	good
CAM-22_NOAA-GFDL-GFDL-ESM2M_RegCM4-7	20.25	good	good	0.643 (0.480 ... 0.808)	-0.22 (-0.71 ... 0.021)	good
CAM-44_CCCma-CanESM2_CRCM5	19.80	good	bad	0.485 (0.344 ... 0.586)	-0.16 (-0.59 ... 0.13)	bad
CAM-44_CCCma-CanESM2_RCA4	19.78	good	good	0.618 (0.343 ... 0.810)	-0.25 (-0.67 ... 0.41)	good
CAM-44_CNRM-CERFACS-CNRM-CM5_RCA4	17.37	good	good	0.898 (0.667 ... 1.08)	-0.39 (-0.74 ... -0.044)	reasonable
CAM-44_CSIRO-QCCCE-CSIRO-Mk3-6-0_RCA4	20.13	good	good	0.569 (0.392 ... 0.682)	-0.090 (-0.59 ... 0.21)	good
CAM-44_ICHEC-EC-EARTH_RCA4	18.12	good	good	0.640 (0.447 ... 0.833)	-0.18 (-0.60 ... 0.25)	good
CAM-44_MIROC-MIROC5_RCA4	19.30	good	good	0.693 (0.537 ... 0.813)	-0.22 (-0.49 ... 0.052)	good
CAM-44_MOHC-HadGEM2-ES_RCA4	19.44	good	good	0.752 (0.601 ... 0.909)	-0.29 (-0.76 ... -0.15)	good
CAM-44_MPI-M-MPI-ESM-LR_RCA4	19.42	good	good	0.540 (0.382 ... 0.664)	-0.14 (-0.43 ... 0.12)	good
CAM-44_NCC-NorESM1-M_RCA4	18.16	good	good	0.505 (0.355 ... 0.745)	-0.14 (-0.66 ... 0.078)	good
CAM-44_NOAA-GFDL-GFDL-ESM2M_RCA4	17.31	good	good	0.559 (0.432 ... 0.682)	-0.20 (-0.46 ... -0.0040)	good
HighResMIP:						
EC-Earth3P-HR	21.38933415	good	good	0.534 (0.360 ... 0.642)	-0.33 (-0.61 ... -0.038)	good
EC-Earth3P	21.39526711	good	good	0.536 (0.373 ... 0.704)	-0.22 (-0.62 ... 0.054)	good
HadGEM3-GC31-HM	20.00005587	good	good	0.556 (0.433 ... 0.653)	-0.23 (-0.63 ... 0.020)	good
HadGEM3-GC31-LM	19.71719618	good	good	0.657 (0.486 ... 0.834)	-0.41 (-0.78 ... -0.11)	good
HadGEM3-GC31-MM	20.05677271	good	good	0.426 (0.266 ... 0.526)	-0.22 (-0.45 ... 0.13)	good
MPI-ESM1-2-HR	24.18680814	good	good	0.812 (0.479 ... 1.08)	-0.45 (-0.76 ... -0.11)	good

Model / Observations	Threshold for return period 2 yr	Seasonal cycle	Spatial pattern	Sigma	Shape parameter	Conclusion
MPI-ESM1-2-XR	24.1459 5398	good	good	0.667 (0.418 ... 0.858)	-0.44 (-0.67 ... -0.18)	good

5 Multi-method multi-model attribution

Tables 5.1 and 5.2 show Probability Ratios (PR) and changes in intensity (ΔI) for observational data products and those models that passed model evaluation. Where a model has been run at several different resolutions (e.g., EC-Earth3P-HR and EC-Earth3P in the HighResMIP ensemble) we retain only the best performing model. Where two models performed equally well, we retain the highest-resolution run.

Table 5.1. Probability ratio and change in intensity for Tx5x: (a) from pre-industrial climate to the present and (b) from the present to 2°C above pre-industrial climate, for the area average.

Model / Observations	a. Past vs. present		b. Present vs. future	
	Probability ratio PR [-]	Change in intensity ΔI [˚C]	Probability ratio PR [-]	Change in intensity ΔI [˚C]
ERA5	13 (2.6 ... ∞)	1.4 (0.70 ... 2.1)		
CPC	61 (2.6 ... ∞)	1.9 (0.60 ... 3.1)		
MSWX	69 (3.2 ... ∞)	2.2 (0.90 ... 3.6)		
ACCESS-CM2	47 (6.2 ... 1.0e+4)	1.3 (0.56 ... 1.9)	0.98 (0.79 ... 1.2)	0.98 (0.79 ... 1.2)
ACCESS-ESM1-5	16 (4.3 ... 1.0e+4)	1.6 (1.0 ... 2.2)	1.0 (0.85 ... 1.2)	1.0 (0.85 ... 1.2)
CanESM5	1.3e+3 (33 ... 1.0e+4)	1.4 (1.1 ... 1.7)	0.91 (0.81 ... 1.0)	0.91 (0.81 ... 1.0)
CMCC-ESM2	58 (7.8 ... 1.0e+4)	1.5 (1.0 ... 2.0)	1.1 (0.94 ... 1.3)	1.1 (0.94 ... 1.3)
EC-Earth3	13 (5.0 ... 2.5e+2)	1.3 (0.97 ... 1.7)	0.94 (0.83 ... 1.1)	0.94 (0.83 ... 1.1)
EC-Earth3-Veg	16 (5.3 ... 1.0e+4)	1.2 (0.72 ... 1.7)	0.82 (0.66 ... 0.99)	0.82 (0.66 ... 0.99)
EC-Earth3-Veg-LR	13 (2.4 ... 1.0e+4)	0.91 (0.31 ... 1.6)	0.83 (0.64 ... 1.0)	0.83 (0.64 ... 1.0)
FGOALS-g3	9.0 (3.1 ... 1.9e+2)	0.95 (0.49 ... 1.4)	0.66 (0.52 ... 0.80)	0.66 (0.52 ... 0.80)
MPI-ESM1-2-HR	1.3e+3 (25 ... 1.0e+4)	2.0 (1.5 ... 2.6)	1.2 (0.98 ... 1.4)	1.2 (0.98 ... 1.4)
MPI-ESM1-2-LR	56 (7.3 ... 1.0e+4)	1.6 (0.99 ... 2.4)	1.0 (0.74 ... 1.3)	1.0 (0.74 ... 1.3)
MRI-ESM2-0	9.8e+2 (15 ... 1.0e+4)	1.6 (0.86 ... 2.2)	1.1 (0.84 ... 1.4)	1.1 (0.84 ... 1.4)
NorESM2-MM	29 (4.7 ... 1.0e+4)	1.4 (0.78 ... 2.1)	1.3 (1.1 ... 1.5)	1.3 (1.1 ... 1.5)
CAM-22_MOHC-HadGEM2-ES_RegCM4-7	32 (3.9 ... ∞)	1.2 (0.43 ... 1.7)	4.6 (3.5 ... 6.2)	0.95 (0.77 ... 1.1)
CAM-22_MPI-M-MPI-ESM-MR_RegCM4-7	19 (3.0 ... ∞)	1.9 (1.4 ... 2.6)	4.3 (2.7 ... 7.0)	1.0 (0.81 ... 1.2)

Model / Observations	Probability ratio PR [-]	Change in intensity ΔI [°C]	Probability ratio PR [-]	Change in intensity ΔI [°C]
CAM-22_NOAA-GFDL-GFDL-ESM2M_RegCM4-7	3.3 (1.1 ... ∞)	1.2 (0.20 ... 2.5)	2.3 (1.6 ... 4.1)	0.81 (0.51 ... 1.2)
CAM-44_MOHC-HadGEM2-ES_RegCM4-3	5.8 (1.7 ... 2.5e+2)	0.85 (0.27 ... 1.3)	3.5 (2.3 ... 5.2)	0.86 (0.69 ... 1.0)
CAM-44_MPI-M-MPI-ESM-MR_RegCM4-3	69 (4.2 ... ∞)	1.4 (0.61 ... 2.1)	4.0 (2.7 ... 6.0)	0.80 (0.56 ... 1.0)
EC-Earth3P	∞ (18 ... ∞)	1.9 (0.89 ... 2.9)	5.9 (4.4 ... 8.3)	1.3 (0.98 ... 1.6)
HadGEM3-GC31-LM	3.0e+2 (9.5 ... ∞)	1.9 (1.0 ... 2.7)	4.9 (3.6 ... 6.9)	1.3 (0.99 ... 1.5)
MPI-ESM1-2-XR ()	∞ (2.8 ... ∞)	1.2 (0.19 ... 2.0)	6.9 (5.1 ... 8.9)	1.1 (0.72 ... 1.2)

Table 5.2. Probability ratio and change in intensity for Tn5x: (a) from pre industrial climate to the present and (b) from the present to 2°C above pre industrial climate, for the area average.

Model / Observations	a. Past vs. present		b. Present vs. future	
	Probability ratio PR [-]	Change in intensity ΔI [°C]	Probability ratio PR [-]	Change in intensity ΔI [°C]
ERA5	37 (8.5 ... 5.6e+4)	1.4 (0.94 ... 1.8)		
CPC	1.2e+3 (49 ... ∞)	2.5 (1.5 ... 3.4)		
MSWX	∞ (∞ ... ∞)	3.5 (1.7 ... 3.1)		
ACCESS-CM2	1.6e+2 (7.2 ... 1.0e+4)	1.4 (0.84 ... 2.0)	2.0 (1.6 ... 2.3)	1.1 (1.0 ... 1.2)
ACCESS-ESM1-5	31 (11 ... 8.4e+2)	1.6 (1.2 ... 2.1)	2.0 (1.7 ... 2.4)	1.0 (0.92 ... 1.1)
CanESM5	∞ (98 ... 1.0e+4)	1.8 (1.3 ... 2.2)	2.0 (1.7 ... 2.4)	0.98 (0.92 ... 1.0)
CMCC-ESM2	16 (2.9 ... 5.8e+3)	1.1 (0.48 ... 1.7)	2.0 (1.7 ... 2.4)	0.89 (0.79 ... 0.98)
EC-Earth3	1.0e+4 (34 ... 1.0e+4)	1.9 (1.3 ... 2.3)	1.9 (1.7 ... 2.2)	1.0 (0.93 ... 1.1)
EC-Earth3-Veg	82 (15 ... 1.0e+4)	1.9 (1.3 ... 2.5)	1.9 (1.6 ... 2.2)	0.98 (0.89 ... 1.1)
EC-Earth3-Veg-LR	13 (3.5 ... 5.0e+3)	1.3 (0.66 ... 2.0)	1.9 (1.7 ... 2.3)	1.1 (0.95 ... 1.2)
FGOALS-g3	2.8e+2 (13 ... 1.0e+4)	1.9 (1.2 ... 2.6)	1.9 (1.6 ... 2.2)	0.88 (0.78 ... 1.0)
INM-CM4-8	1.0e+4 (1.6e+2 ... 1.0e+4)	1.9 (1.4 ... 2.4)	2.0 (1.5 ... 2.7)	1.0 (0.82 ... 1.2)
INM-CM5-0	1.0e+4 (1.8e+2 ... 1.0e+4)	1.7 (1.1 ... 2.4)	2.0 (1.6 ... 2.6)	1.1 (1.0 ... 1.2)
MPI-ESM1-2-HR	1.2e+3 (12 ... 1.0e+4)	1.9 (0.93 ... 2.9)	1.9 (1.7 ... 2.3)	1.3 (1.1 ... 1.5)
MPI-ESM1-2-LR	2.5 (0.42 ... 50)	0.65 (-0.58 ... 1.9)	1.9 (1.6 ... 2.2)	1.2 (0.99 ... 1.4)
MRI-ESM2-0	8.1 (2.5 ... 85)	1.2 (0.53 ... 1.9)	1.8 (1.6 ... 2.1)	0.96 (0.80 ... 1.1)
NorESM2-MM	56 (15 ... 1.0e+4)	1.9 (1.3 ... 2.5)	2.0 (1.7 ... 2.3)	1.1 (0.98 ... 1.2)
CAM-22_MOHC-HadGEM2-ES_RegCM4-7	25 (6.1 ... ∞)	1.3 (0.91 ... 2.0)	1.9 (1.8 ... 2.0)	0.90 (0.78 ... 1.0)
CAM-22_MPI-M-MPI-ESM-MR_RegCM4-7	6.4e+2 (12 ... ∞)	1.6 (1.1 ... 2.2)	1.9 (1.8 ... 2.0)	1.0 (0.82 ... 1.2)
CAM-22_NOAA-GFDL-GFDL-ESM2M_CRCM5	4.7e+3 (23 ... ∞)	1.4 (0.87 ... 1.8)	2.0 (2.0 ... 2.0)	1.2 (1.0 ... 1.3)
CAM-22_NOAA-GFDL-GFDL-ESM2M_RegCM4-7	22 (3.4 ... ∞)	1.5 (0.73 ... 2.2)	1.9 (1.8 ... 2.0)	1.2 (0.93 ... 1.4)
CAM-44_CCCma-CanESM2_RCA4	23 (8.7 ... ∞)	1.5 (1.2 ... 1.8)	1.9 (1.8 ... 2.0)	0.96 (0.84 ... 1.1)
CAM-44_CSIRO-QCCCE-CSIRO-Mk3-6-0_RCA4	1.1e+2 (20 ... ∞)	2.1 (1.2 ... 2.6)	2.0 (1.9 ... 2.0)	1.3 (1.1 ... 1.5)

	a. Past vs. present		b. Present vs. future	
CAM-44_ICHEC-EC-EARTH_RCA4	1.7e+2 (9.4 ... ∞)	1.8 (1.3 ... 2.3)	1.9 (1.8 ... 2.0)	1.1 (0.94 ... 1.2)
CAM-44_MIROC-MIROC5_RCA4	16 (4.0 ... ∞)	1.4 (0.85 ... 2.0)	1.9 (1.8 ... 2.0)	1.1 (0.95 ... 1.3)
CAM-44_MOHC-HadGEM2-ES_RCA4	13 (3.5 ... ∞)	1.2 (0.80 ... 1.7)	1.9 (1.8 ... 1.9)	0.95 (0.85 ... 1.1)
CAM-44_MPI-M-MPI-ESM-LR_RCA4	1.3e+2 (26 ... ∞)	1.7 (1.3 ... 2.0)	2.0 (1.9 ... 2.0)	1.1 (0.98 ... 1.3)
CAM-44_NCC-NorESM1-M_RCA4	7.5e+2 (43 ... ∞)	1.9 (1.5 ... 2.3)	2.0 (1.9 ... 2.0)	1.1 (0.93 ... 1.3)
CAM-44_NOAA-GFDL-GFDL-ESM2M_RCA4	2.5e+2 (12 ... ∞)	1.6 (1.0 ... 2.0)	2.0 (1.9 ... 2.0)	1.2 (1.0 ... 1.4)
EC-Earth3P-HR	∞ (2.4e+4 ... ∞)	2.3 (1.7 ... 2.7)	2.0 (1.9 ... 2.0)	1.2 (1.0 ... 1.4)
HadGEM3-GC31-HM	2.7e+2 (12 ... ∞)	1.5 (1.1 ... 2.0)	2.0 (1.9 ... 2.0)	1.1 (0.98 ... 1.3)
MPI-ESM1-2-XR	∞ (1.2e+2 ... ∞)	2.0 (1.4 ... 2.7)	1.9 (1.8 ... 2.0)	1.2 (1.0 ... 1.3)

6 Hazard synthesis

For the event definitions described above we evaluate the influence of anthropogenic climate change on the events by calculating the probability ratio as well as the change in intensity using observations and climate models. Models which do not pass the evaluation described above are excluded from the analysis. The aim is to synthesise results from models that pass the evaluation along with the observations-based products, to give an overarching attribution statement.

Figures 10-13 show the changes in probability and intensity for the observations (blue) and models (red). Before combining them into a synthesised assessment, first, a representation error is added (in quadrature) to the observations, to account for the difference between observations-based datasets that cannot be explained by natural variability. This is shown in these figures as white boxes around the light blue bars. The dark blue bar shows the average over the observation-based products. Next, a term to account for intermodel spread is added (in quadrature) to the natural variability of the models. This is shown in the figures as white boxes around the light red bars. The dark red bar shows the model average, consisting of a weighted mean using the (uncorrelated) uncertainties due to natural variability plus the term representing intermodel spread (i.e., the inverse square of the white bars).

Observation-based products and models are combined into a single result in two ways. Firstly, we neglect common model uncertainties beyond the intermodel spread that is depicted by the model average, and compute the weighted average of models (dark red bar) and observations (dark blue bar): this is indicated by the magenta bar. As, due to common model uncertainties, model uncertainty can be larger than the intermodel spread, secondly, we also show the more conservative estimate of an unweighted, direct average of observations (dark red bar) and models (dark blue bar) contributing 50% each, indicated by the white box around the magenta bar in the synthesis figures.

Results are shown in Table 6.1, where differences are presented for changes between the past, 1.2 ℃ cooler climate, and between the present and a future, 0.8℃ warmer climate. Although observational trends do not fully agree quantitatively, partly due to the different lengths, they agree well on the sign of change. Similarly, the models agree well on the qualitative change in both past to present and present to future. Moreover, the observed trends and modelled trends agree quite well, even on the magnitude of change. Therefore we use weighted averages (purple bars) for all measures. Combining lines of evidence from the synthesis results of the past climate, results from future projections and

physical knowledge we communicate the best estimate. We communicate a PR of about 35 for Tx5x and 200 for Tn5x, and note that these trends continue into the future, with a PR of another 4 times for Tx5x and another 2 times for Tn5x. It is important to highlight though, that given the return time of Tn5x is 2 in today's climate, the probability ratio cannot increase further than a doubling as an annual index cannot occur more frequently than once a year. The intensity change between past and present for Tx5x is about 1.4℃, and for Tn5x this is about 1.6℃. This continues into the future with another one degree for both Tx5x and Tn5x.

Periods	Data	Tx5x		Tn5x	
		Probability ratio (95% CI)	Intensity change (%) (95% CI)	Probability ratio (95% CI)	Intensity change (%) (95% CI)
Past-Present	Observations	38.00 (1.678 ... 744727)	1.869 (0.5269 ... 3.260)	517.3 (2.406 ... 8547432)	2.496 (0.07841 ... 4.669)
	Models	34.26 (8.296 ... 182.1)	1.382 (1.061 ... 1.7040)	178.6 (5.950 ... 5593)	1.639 (1.461 ... 1.814)
	Synthesis (Observations & Models)	34.45 (8.906 ... 182.4)	1.408 (1.095 ... 1.721)	214.2 (11.03 ... 5823)	1.644 (1.467 ... 1.818
Present-Future	Synthesis (Models only)	4.237 (3.038 ... 5.965)	0.9790 (0.7185 ... 1.240)	1.963 (1.942 ... 1.978)	1.061 (0.8919 ... 1.231)

Table 6.1: Summary of results for Tx5x (left) and Tn5x (right), presented in Figs 9-12: changes due to GMST include past-present changes and present-future. All values are statistically significant.
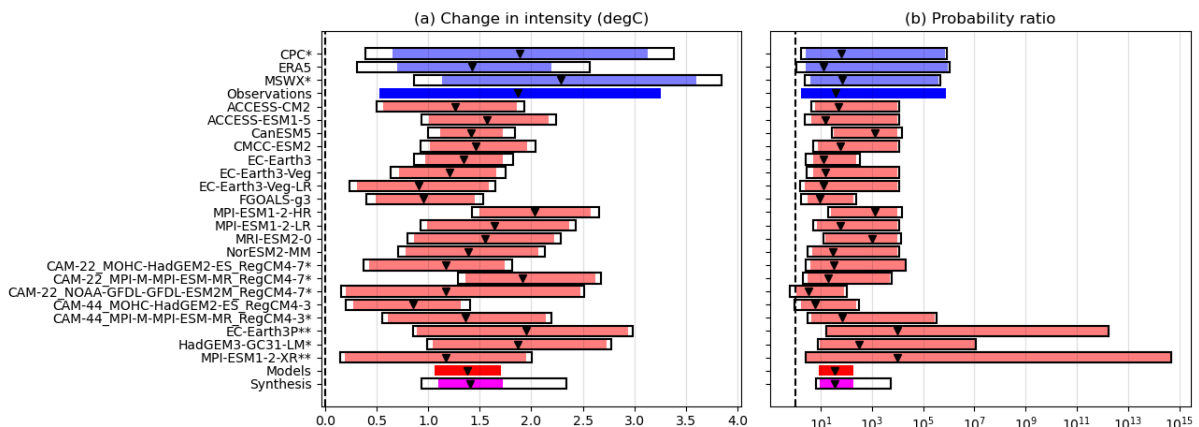

Figure 10: Synthesis of change in intensity (°C) in May-June Tx5x between (a) and probability ratios (b) in the current climate compared with a 1.2C cooler climate. Data sets marked with a * originally had an infinite upper bound, which was replaced with a value representing a 6-sigma interval based on the finite best estimate and lower bound. Models marked with ** originally also had an infinite best estimate, which was first replaced with the largest finite upper bound among all models, before a 6-sigma upper bound was estimated.
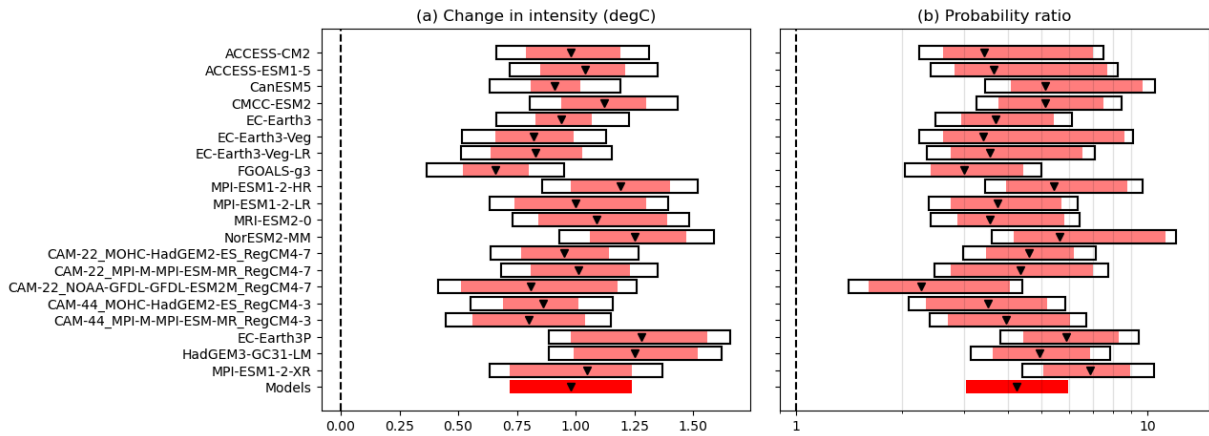
Figure 11: Synthesis of change in intensity (°C) in May-June Tx5x between (a) and probability ratios (b) in the current climate compared with a 0.8C warmer climate (ie. with total warming of 2C)
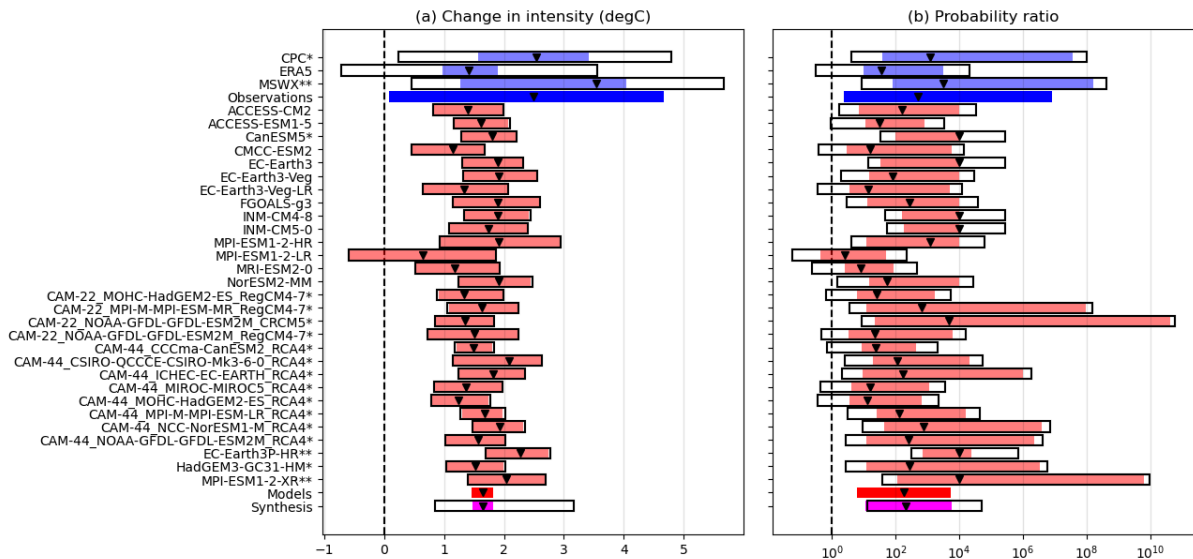

*Figure 12: Synthesis of change in intensity (°C) in May-June Tn5x between (a) and probability ratios (b) in the current climate compared with a 1.2C cooler climate. Data sets marked with a * originally had an infinite upper bound, which was replaced with a value representing a 6-sigma interval based on the finite lower bound of that data set. Models or observational data sets marked with ** originally also had an infinite best estimate, which was first replaced with the largest finite upper bound among all models or among all observational data sets respectively, before a 6-sigma upper bound was estimated.*
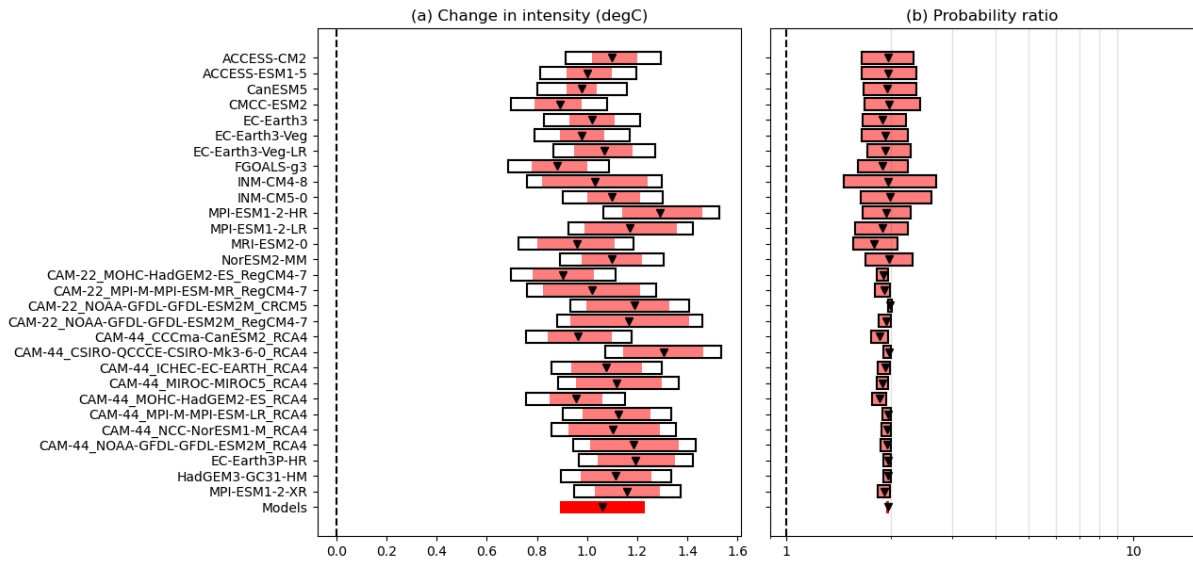
Figure 13: Synthesis of change in intensity (°C) in May-June Tn5x between (a) and probability ratios (b) in the current climate compared with a 0.8C warmer climate (ie. with total warming of 2C)

7 Vulnerability and exposure

Extreme heat events are increasingly becoming a critical concern across the globe, affecting millions and posing substantial risks to human health, livelihoods, and infrastructure. This section outlines factors that drive vulnerability and exposure in the United States (U.S.) Southwest, Mexico, and parts of Central America, noting that there are vast differences in capacity, awareness, and impacts in these places.

Vulnerability across the region is particularly pronounced among outdoor workers, including agricultural labourers and miners, who face direct exposure and strenuous conditions exacerbated by heat stress (Lin et al., 2024). Unhoused populations, pregnant individuals, young children, and older adults are also at heightened risk due to physiological factors and limited access to cooling facilities (Yglesias- González et al., 2022). Incarcerated populations and guards in facilities lacking adequate cooling further highlight systemic inequities exacerbated by extreme heat (Skarha et al., 2022; Terwiel, 2018). Furthermore, refugees and migrants in transit are also particularly vulnerable, due to the often long, dangerous, and physiologically heavy journey, high exposure to temperatures, and limited coping capacity (Amaral, 2024; Singh, 2024). Beyond physical health impacts, extreme heat poses risks to psychosocial health, with increased incidence of anxiety, depression, irritability, sleep disruption, cognitive impairment, aggression, and suicidal ideation (Rony & Alamgir, 2023; Pinchoff et al., 2023). Across the US and Mexico, suicide rates increase by 0.7% and 2.1%, respectively, for every 1C increase in monthly average temperature (Burke et al., 2018). Overall, these vulnerabilities intersect with socioeconomic factors such as poverty, occupational hazards, and historical policies influencing housing conditions and healthcare access.

Previously rare occurrences of extreme heat are now more frequent across the spatial domain, with maximum and minimum temperatures showing a 15 and 2-year return period, respectively, reflecting

a trend towards higher frequency, severity, and duration. These changes are already exacerbating long-term health impacts and strain critical sectors like agriculture, water resources, and energy (Arsht, 2021). Understanding the key drivers of heat risk, along with risk mitigating factors, is crucial for effective risk management and adaptation strategies. This vulnerability and exposure analysis will delve deeper into and offer insights on the facets of vulnerability, exposure and coping capacity to extreme heat across the study region.

7.1 Informality and urban planning for heat

In high-income countries, heat is predominantly addressed as a health issue, especially in urban settings. Conversely, in low and middle-income countries, heat adaptations emphasise agricultural and livelihood impacts, viewing heat primarily as a compound hazard alongside drought and other hydrological threats. According to an Oxford Climate Change research report, the U.S. is one of the most extensively studied countries regarding extreme heat adaptation, while there is a notable lack of analysis on extreme heat adaptation in Latin America and the Caribbean (Tuek-Hankins et al., 2021).

Urban centers tend to concentrate heat impacts, in part, due to higher temperatures due to the urban heat island effect. Urban populations are currently estimated at 108 million in Mexico and 31 million in Central America (de Sherbinin et al., 2020). Projected growth in urban areas in the region is consistent across three future scenarios, increasing from 90 million people in 2010 to approximately 140 million by 2050. This growth is accompanied by urban sprawl through land-use changes to tackle rapid urbanisation, the loss of natural reserves, and a rise in informal settlements (Lustgarten, 2020), a dynamic that has contributed to a heat island effect. Home to over 400,000 people, more than 2,000 informal settlements along the Texas-Mexico border, called *Colonias*, are notably vulnerable due to poor housing conditions, lack of access to basic services and infrastructure, and social and physical isolation (Durst, 2013).

Urban heat islands are a byproduct of the built environment, causing cities to experience more heat than rural areas because man-made structures like buildings, streets, and sidewalks retain more heat than natural surfaces, further exacerbated by waste heat emissions. In major and mid-sized cities in Mexico and Central America there has been a significant deterioration of natural spaces and changes in land use on a large scale, which is related to both informal and formal growth, gravely damaging existing ecosystems, generating significant losses in biodiversity (ECLAC, 2014). Despite a fair proportion of the region's territories being officially declared protected areas, there are many challenges derived from the financial, technical, and human resources limitations to guaranteeing the enforcement of these regulations.

These cities also suffer from high levels of congestion and high motorization rates which contribute to air pollution to further exacerbate health impacts when combined with extreme heat (de Sherbinin et al., 2020). Los Angeles is known for having one of the most intense heat islands in the world: temperatures in the city centre can exceed 5°C higher than in adjacent areas. The urban typology is a determining factor. The centres of North American cities, with greater concentration and height of buildings and less trees, generate greater heat islands (We Are Water, 2023). The month of May 2024 recorded a new all-time high for Mexico City, with 34.2C, which is markedly higher than the June

Tmax average of 23.5C (Weather Atlas, n.d.). Extreme temperatures have already caused deaths in Mexico, occurring mainly in cities (El País, 2024).

Certain neighbourhoods and population groups are disproportionately affected by urban heat. Low-income populations are more likely to reside in hotter areas and face higher air pollution levels than those in wealthier neighbourhoods, partly due to higher densities and the unequal distribution of green spaces (Grinspan et al., 2020). They are also more susceptible to health issues caused by heat waves and stormwater flooding, among other compounded climate change impacts. Furthermore, informal settlements, which constitute about 29% of the urban population in Central America (EUROsociAL, 2021), typically have houses made from low-cost materials like tin sheets roofs. These houses often have poor ventilation and insulation, offering little protection from heat stress (Ramsay et al., 2024).

The city's problems demonstrate the connection between the historical processes of transformation, power and access to the city's resources, and shed light on the issue of vulnerability. In particular, women are among the most vulnerable groups in the region along with indigenous communities characterised for having a lack of access to basic services and infrastructure. The urban poor are also more likely to work in occupations requiring outdoor and physical labour, and they often aren't provided labour and social protections (Mackres et al., 2023).

7.2 Water, electricity, and health systems

Sustained, high temperatures can reduce the capacity and efficiency of electricity generation. This is compounded by an increased burden on electricity grids through the expanded use of cooling infrastructure (Birol, 2021). When heatwaves impact broader regions, there is reduced capacity to draw on neighbouring countries for power generation (ibid.). Generally, Mexico faces constrained coping capacity due to socio-economic factors of vulnerability and uneven distribution of urban services (ECLAC, 2014). At the end of 2023, The dams of the Cutzamala system were at 30% of their capacity at the end of 2023, with the reservoir levels further affected by the heat dome of 2024. Subsequently, a water security crisis was triggered in the capital (Zambrano, 2024). The water supply for large cities is at risk from the same drought as 80% of the territory suffered a certain degree of drought this season (MSM, 2024), which could challenge a water supply system that is already being outpaced by urban growth. In Mexico, this led to rolling blackouts across 20 of 32 states, with the national grid declaring a state of emergency at least twice by early May (Alire Harcia & Barrera, 2024; Navarro, 2024). High temperatures have caused the population to resort to cooling systems, mostly electric, which has resulted in higher energy consumption and impacted household spending (El Economista, 2024). With Mexico's urban population expected to surge by 2050, measures under Mexico City's Climate Action Plan aim to mitigate climate risks and manage increasing cooling demands. Similarly in Honduras, blackouts impacted urban centres for two up to hours at a time (Tico Times, 2024). While the majority of Mexico's population is urban, rural healthcare access is still a significant barrier, notably for indigenous individuals and older adults (Carrillo-Balam et al., 2020).

The electricity system of Texas is particularly vulnerable to failure as it relies on it's own grid while other States are relying on one of two other systems (Hao, 2024). Moreover, the State has a deregulated power market which saw an increase of prices by 1600% in early May due to higher energy demands (Ma, 2024). A recent survey in Texas found that 33% of Texans have paid their

electricity bills late at least once in the last 12 months, with 7% indicating that their accounts were escalated to a collections agency (Nogueras Ramos, 2024). Individuals in the State who are unable to pay their power bill may apply to the Comprehensive Energy Assistance Program, a program which helps low-income households with financial assistance to pay for energy bills (Nogueras Ramos, 2024; Benefits.gov, n.d.). However to qualify, households must be 150% below the Federal Poverty Guidelines (Nogueras Ramos, 2024). This leaves a significant gap in assistance for individuals who are low-income but do not meet the threshold.

Heatwaves also threaten water systems, especially when compounded by droughts as was the case in many of the focus countries. Water storage levels in the Cutzamala system are reported to be critically low at 31% threatening a major source of drinkable water (Alire Harcia & Barrera, 2024). In May, there were approximately 20 million individuals dealing with intermittent water supply due to low rainfall (Navarro, 2024).

Information on the impact of health systems is currently quite limited. However, a number of heat-related illnesses such as heat stroke and heat exhaustion, are likely to have occurred over the region during this period. In the US, some areas are piloting alternative approaches for heat stroke while transporting individuals to health centers, such as ice immersion (Snow, 2024). Alternative policies include introducing heat safety protection for outdoor workers. It is evident that prolonged heat events are stressing systems that are not designed to deal with chronic heat, further compounded by major population growth in high risk communities in states such as Arizona and Texas.

7.3 Agriculture

Agricultural workers face significant vulnerabilities due to heat exposure, with farmworkers in the U.S. being twenty times more likely to die from heat-related causes compared to other workers (Kaleikini, 2024). Heat exposure in the agricultural sector is responsible for up to 2,000 worker fatalities and 170,000 heat-related injuries annually in the US, with a 1% increase in workplace injuries for every 1°C increase in temperature (Kaleikini, 2024). In Central America, particularly among sugarcane workers, there is an epidemic of chronic kidney disease attributed to excessive heat exposure and dehydration, coupled with strenuous physical labour (Bodin et al., 2016; Khayat et al., 2022). This phenomenon is particularly prevalent in Guatemala and El Salvador (Khayat et al., 2022), where workers performing more strenuous tasks, such as cane cutting and pesticide application, show higher rates of impaired kidney function (Petropolous et al., 2023).

Migrant agricultural workers in regions like Sonora, Mexico, also face extreme heat exposure. These workers, often from poorer regions of Southern Mexico, are particularly vulnerable due to their socioeconomic status and lack of alternatives (Wagoner et al., 2020). Studies have highlighted the need for targeted interventions to improve hydration and prevent heat stress, as a significant number of these workers are dehydrated post work-shifts (Wagoner et al., 2020). Despite the effectiveness of simple measures centred on increasing water, rest, and shade (Bodin et al., 2016), barriers such as the piece-rate compensation system, lack of interest from employers, and insufficient regulations hinder their implementation (Chicas et al., 2021).

Effective cooling interventions must consider workers' perceptions and practicalities. For instance, bandanas have been well-received for their practicality, while cooling vests received mixed reviews

regarding their feasibility at work (Chicas et al., 2021). Some of the farmworkers themselves advocate for more frequent rest breaks, shaded areas, personal cooling gear, and heat stress prevention training (Chicas et al., 2021). However, the economic burden of purchasing cooling devices is often beyond their financial reach.

The agricultural sector itself is vulnerable to extreme heat, which affects crop yields, pollinator health, and overall food security (Yglesias-González et al., 2022). Extreme heat events have been shown to decrease planting areas, as observed among subsistence farmers in Peru (Aragón et al., 2018). In Mexico corn production fell by 50% during 2023. Rising global temperatures are expected to significantly reduce the yields of staple grains such as maize and wheat. Additionally, the suitability for coffee cultivation, a key crop in the regional economy, is projected to decline (ECLAC/FAO, 2018). Compound effects of drought and heat exacerbate vulnerabilities, leading to crop failures and increased disease vectors, thus threatening food security (Kaleikini, 2024). In Mexico, periods of drought and declining agricultural productivity drive significant migration to the U.S. (Feng, Krueger, Oppenheimer, 2010). Insect pollinators face heightened vulnerability owing to extreme temperatures, reduced water availability, and additional compounding hazards, underscoring the imperative for policies aimed at stabilising global warming, bolstering local habitat preservation, and enhancing public awareness on the importance of pollinators (Johnson et al., 2023).

To mitigate these impacts and threats, there is a critical need for unified heat safety regulations across states, as exemplified by legislative actions in California, and to address the socioeconomic vulnerabilities of migrant workers who face heightened risks and fear of retaliation (Kaleikini, 2024). Investing in worker safety not only protects health but also offers significant economic benefits by reducing lost productivity (Kaleikini, 2024).

7.4 Heat governance

Government heat action planning and individual response capabilities vary significantly across the study region including the United States, Mexico, and Central America, reflecting stark disparities in resources and infrastructure. Even within the U.S., there are notable differences in heat preparedness and awareness between states. This disparity underscores the broader challenge of addressing climate-induced health risks in an equitable manner across diverse socioeconomic and political landscapes. Furthermore, the full range of preparedness and responses for this heat event across the region is still unknown until further reports come out, and generally heatwave strategies are not always documented. Still, it is clear that in some countries within this region, limited capacity hampers effective responses to extreme heat events. At present, Central America, including Guatemala, Belize, El Salvador, and Honduras, have no early warning systems for extreme heat and no heat action plans (Yglesias-González et al., 2022). A report on extreme heat in Central and South America found that even when warnings for extreme heat are issued across the region, limited actions are taken (ibid.).

In Mexico, the National Meteorological Service (SMN) issued multiple warnings for the extreme heat, stating the third heat wave will end on Tuesday, May 28, and more extreme heat is expected in June (Crisis24, 2024; BanderasNews, 2024). Due to the extreme temperatures, together with high levels of air pollution, the authorities have restricted car use, and advised Mexico City's residents to limit outdoor activities, avoid (outdoor) physical activity, and refrain from refuelling vehicles in the

afternoon ([Le Monde, 2024](#)). Although no formal heat action plan is in place, various response measures have taken place during previous heat events. In addition, research is currently being conducted to co-develop, test, and evaluate a user-driven heat-health action plan across six rural communities in southern Mexico ([ECU, 2023](#)). This will also include an early warning and surveillance system, capacity building, prevention education and communication tools. In addition, the Commission for Environmental Cooperation is developing a real-time heat event surveillance system. During last year's heatwave across Mexico, local governments decided on response measures, which were adapted by the Mexican Red Cross state delegations to fit specific needs of the local population ([Mangones, 2024](#)). Different states took actions such as public awareness campaigns, installing drinking fountains and shade shelters, and adjusting school schedules. A focus was also put on monitoring heatwave alerts and preparedness. Another example of limited capacity building includes Monterrey's Chief Heat officer, who was in place from 2022 to 2023 ([Arsht-Rock, n.d.](#)) and worked on building awareness as well as investments in the built environment. Monterrey became the first City Champion for Heat Action (CCHA) for Mexico and Central America. In addition, other cities such as Mérida encouraged citizen participation in reforestation and developed digital tools for urban tree management ([Arsht-Rock, n.d.](#)). Such actions are crucial, as some people have limited options to adapt. For example, most residents within the metropolitan area of Mexico's City do not own air conditioners, and where other means such as fans are available, these are not sufficient to maintain thermal comfort ([Reuters, 2024](#)).

Across the US, the National Weather Service (NWS) Climate Prediction Centre provides various forecast products to understand forecasted extreme heat anomalies ([NWS CPC, n.d.](#)). This event was forecast and communicated well in advance, with the NWS warning for the heat already on Tuesday May 28 for the interior West. The NWS also has a HeatRisk tool which provides a forecast risk of heat-related impacts to occur for the coming 7 days ([NWS, n.d.](#)). In addition, the US Centers for Disease Control and Prevention (CDC) has a Heat & Health tracker, which provides real-time health information, showing how heat is affecting counties, populations that are at risk, and resources for response ([CDC, n.d.](#)).

Next to the warnings, significant efforts around capacity and preparedness for extreme heat have been taken across the historically warmer regions of the U.S. The Climate-Ready States and Cities Initiative (CRSCI) has supported 16 states across the US, including Arizona and California, to develop health adaptation plans and address gaps. Phoenix, Arizona has a chief heat officer who has directed the city's Office of Heat Response and Mitigation since 2022. Recently, as of 1 March 2024, the U.S.'s first state-level chief heat officer was appointed, who oversees the Extreme Heat Preparedness Plan also released in March ([Office of the Governor, 2024](#)). This plan emphasises preparedness for extreme heat, using innovative approaches to expand and improve cooling centres across the state, including mental health support. At the moment, Maricopa and Pima counties have the most cooling centres, which can be viewed on an ArcGIS map[1]. Furthermore, various Phoenix city departments collaborated to create consistent messages and heat safety signs for hikers ([Hines, 2020](#)). The Arizona Department of Health Services provides an email or text subscription service, which residents and schools can sign-up for to receive heat alerts ([ibid.](#)). Furthermore, Phoenix and Tucson

---

[1] Interactive map of cooling centers, hydration stations, and collection/donation sites in Maricopa, Pima and Yuma counties, available through:
https://adhsgis.maps.arcgis.com/apps/webappviewer/index.html?id=72e37c9bd31841da8396e8d86dc1d665&extent=-12811842.886%2C3756585.9878%2C-12278312.4286%2C4014943.1434%2C102100

have passed heat safety labour laws for city workers and contractors (City of Tuscon, 2024; Rolfsen, 2024). Tucson also recently passed a new Heat Action Roadmap (ibid.)

Los Angeles also has a chief heat officer in place from 2022 (YCC Team, 2022). During periods of extreme heat, cooling centres are opened in various locations, such as LA City's Recreation and Parks' facilities (pet-friendly) and public libraries. These are widely promoted through social media and a phone-line (311) that can refer residents to the cooling facilities. The LA Department of Transportation offers air-conditioned transport to such locations (LA City, n.d.). Furthermore, people can sign-up for emergency heat notifications. Earlier in 2019, the LA Department of Water and Power installed free hydration stations within the city.

Cities in New Mexico have also begun opening cooling centres for community members in recent years, and the state passed a Climate Adaptation and Resilience Plan in March 2024 that has several focus areas including human health and wellness (Adaptation International et al., 2024).

Across Texas, during last year's heat in 2023, the American Red Cross and Central & South Texas Region observed a targeted outreach campaign to help the 9.4 million residents they serve to understand and mitigate the risks posed by extreme heat conditions (Mangones, 2024). Various states have established workplace heat safety standards. Despite these steps forward, in Texas, a law was passed in 2023 to preempt local governments from advancing heat safety labour laws for regular breaks and water (Marr, 2024).

7.5 V&E conclusions

The 2024 early summer heatwave, exacerbated by forest fires and drought conditions, severely impacted the U.S. Southwest, Mexico, and parts of Central America. The heat results in increased healthcare costs, reduced labour productivity, and heightened mortality rates. These impacts are disproportionately affecting vulnerable groups, notably including outdoor workers, the unhoused, low-income residents, and marginalised populations including e.g. indigenous communities.

In urban contexts, poor housing conditions, limited access to cooling services, heat islands, and informal settlements intensify heat impacts, particularly in Mexico and Central America. Government heat action planning and individual response capabilities vary significantly across the United States, Mexico, and Central America, reflecting stark disparities in resources and infrastructure. Even within the U.S, there are notable differences in heat preparedness and awareness between states. The studied countries within Central America have no heat governance systems. Further, across the studied area, water and electricity systems are not resilient to the compounding shocks experienced with the hot-dry events.

Extreme heat warning systems and action plans can help fill critical gaps in preparedness across Central America. Heat safety protection laws can be strengthened or implemented to protect outdoor workers across all countries. Further, strengthened grid resilience and water conservation strategies are critical to ensure reliable services during heat events. Improved urban planning, more green spaces, and enhanced infrastructure in informal settlements will also help protect the most vulnerable.

Data availability

All time series used in the attribution analysis are available via the Climate Explorer.

References

All references are given as hyperlinks in the text.
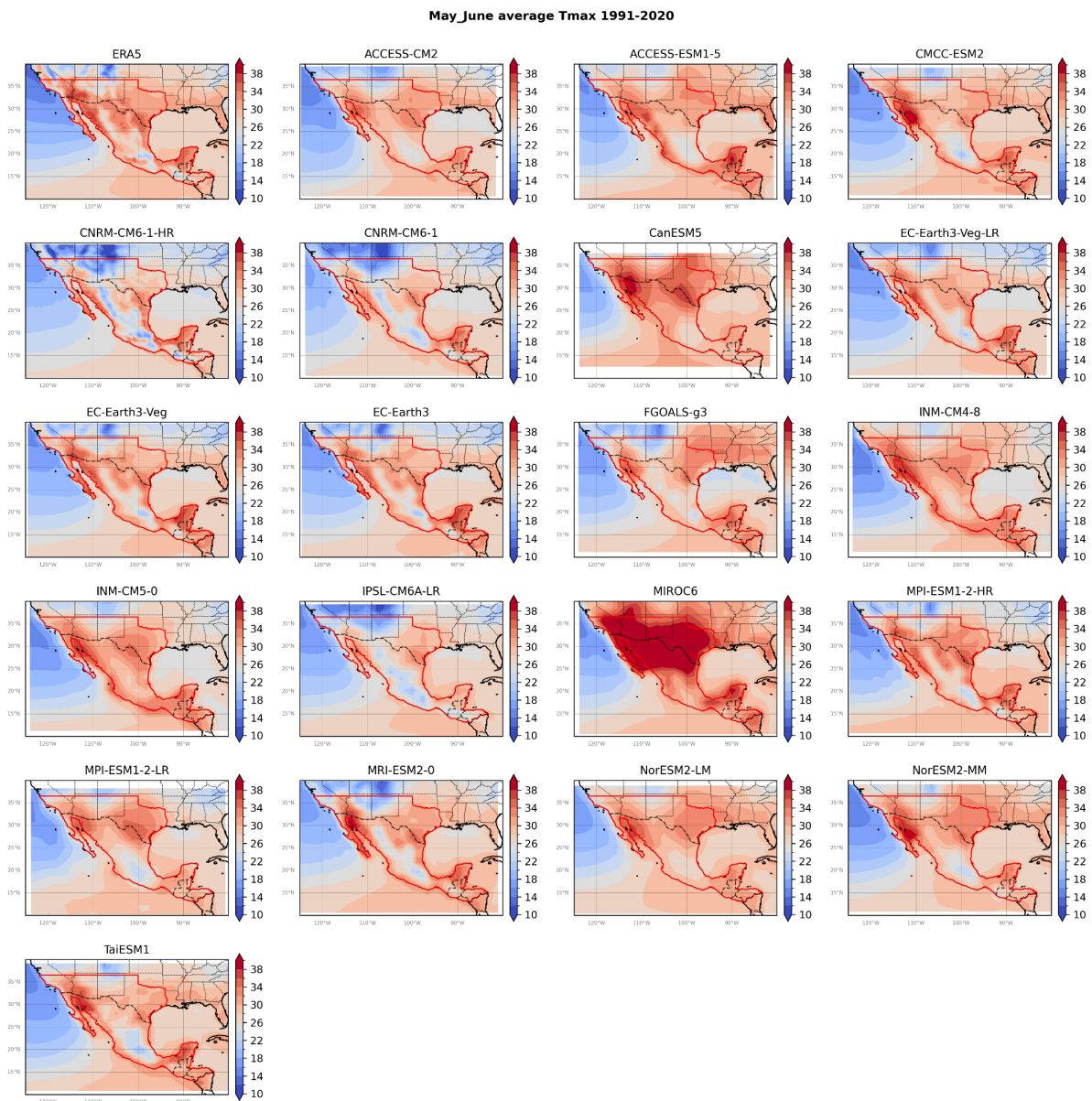
Appendix

Figure A1. Average maximum temperature for May-June over a climatological period of 1991-2020 of ERA5 and CMIP6 models
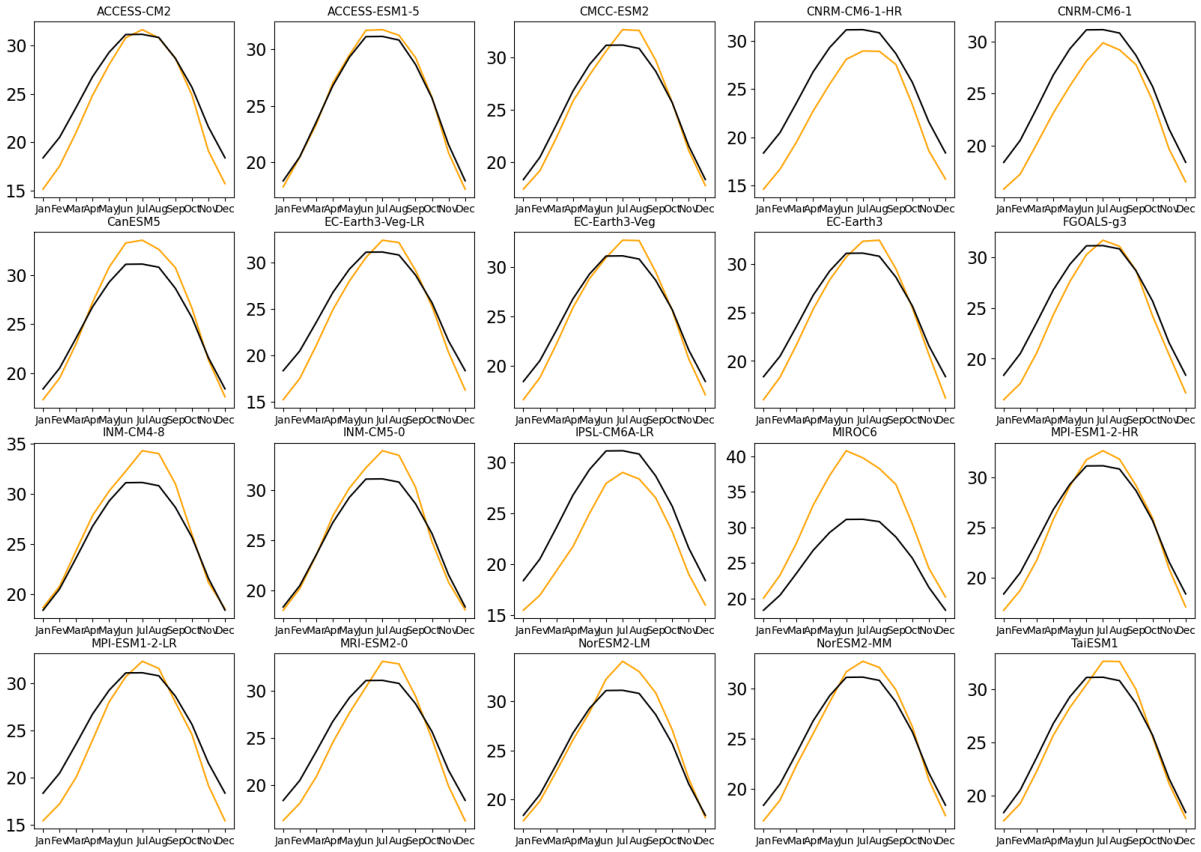
Figure A2: Seasonal cycle of maximum temperature over a climatological period of 1991-2020 of ERA5 and CMIP6 models over the study area .
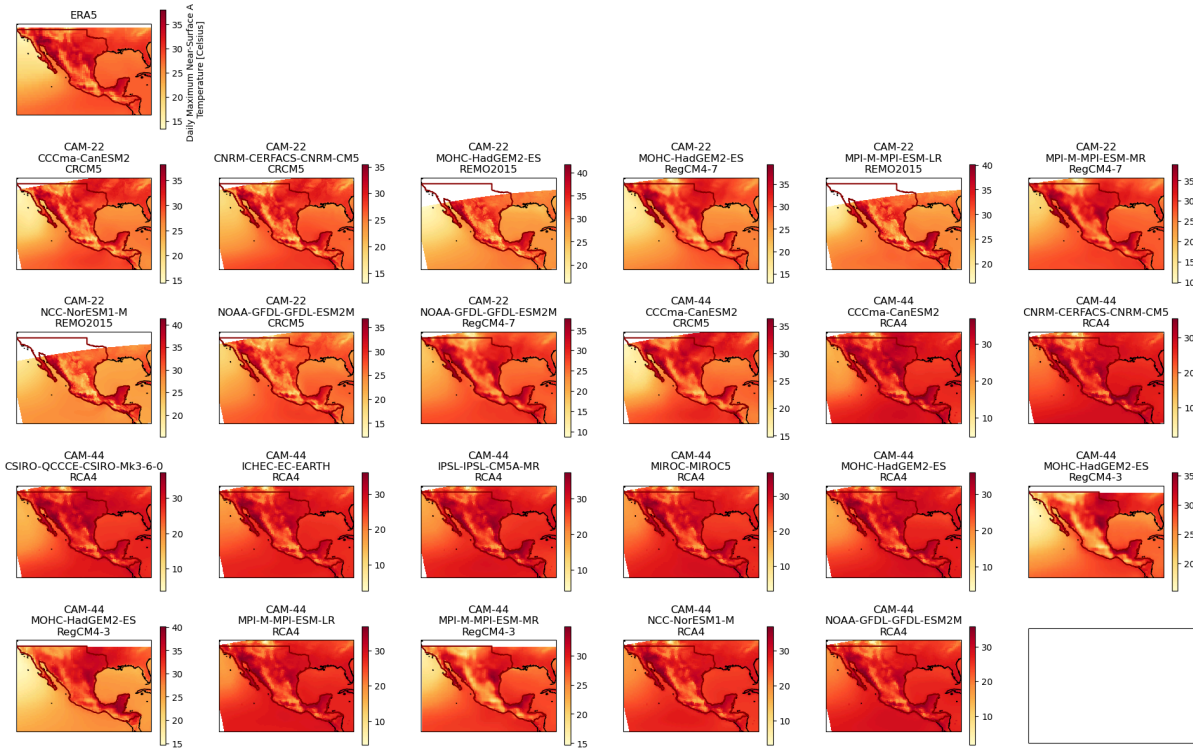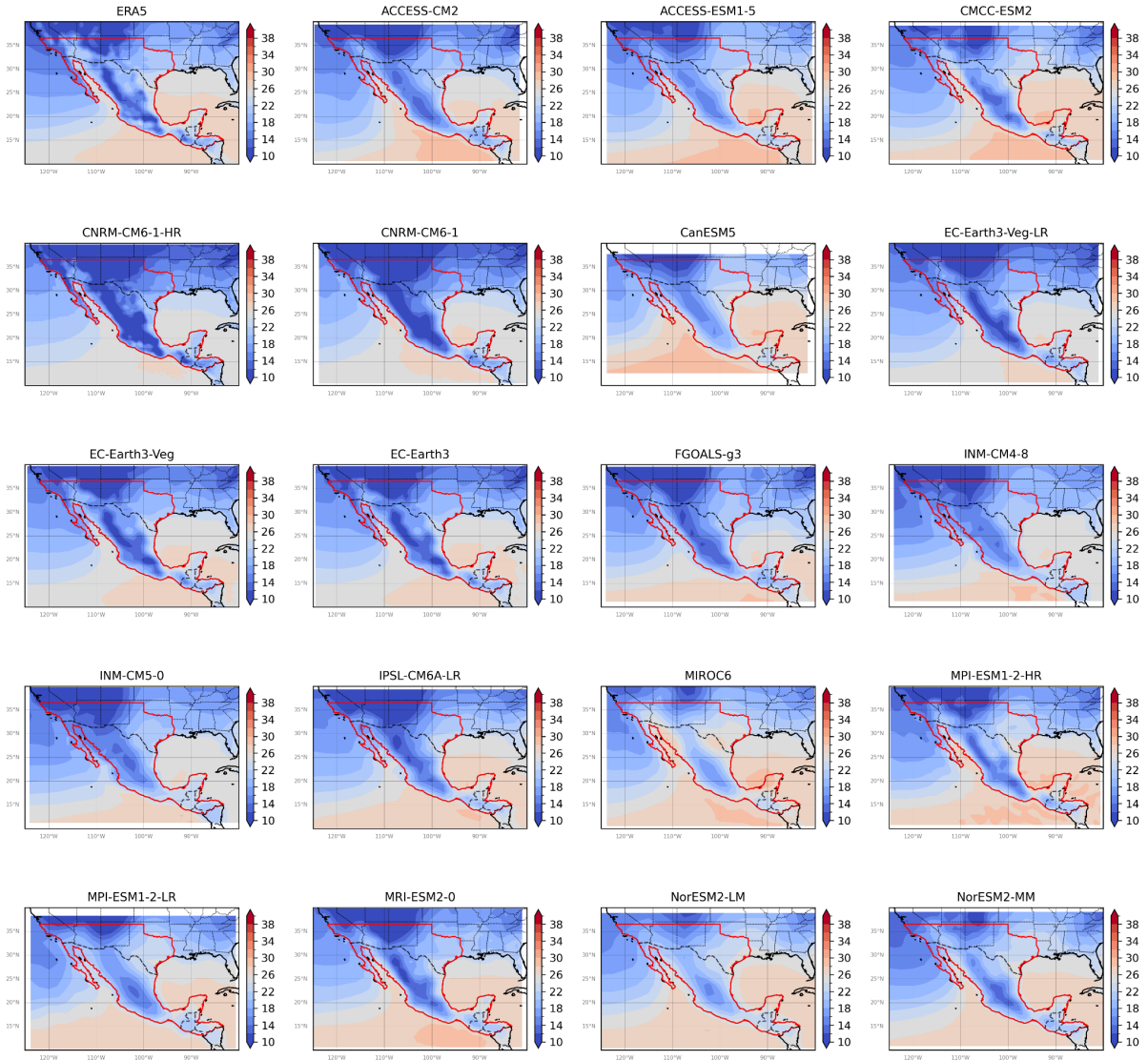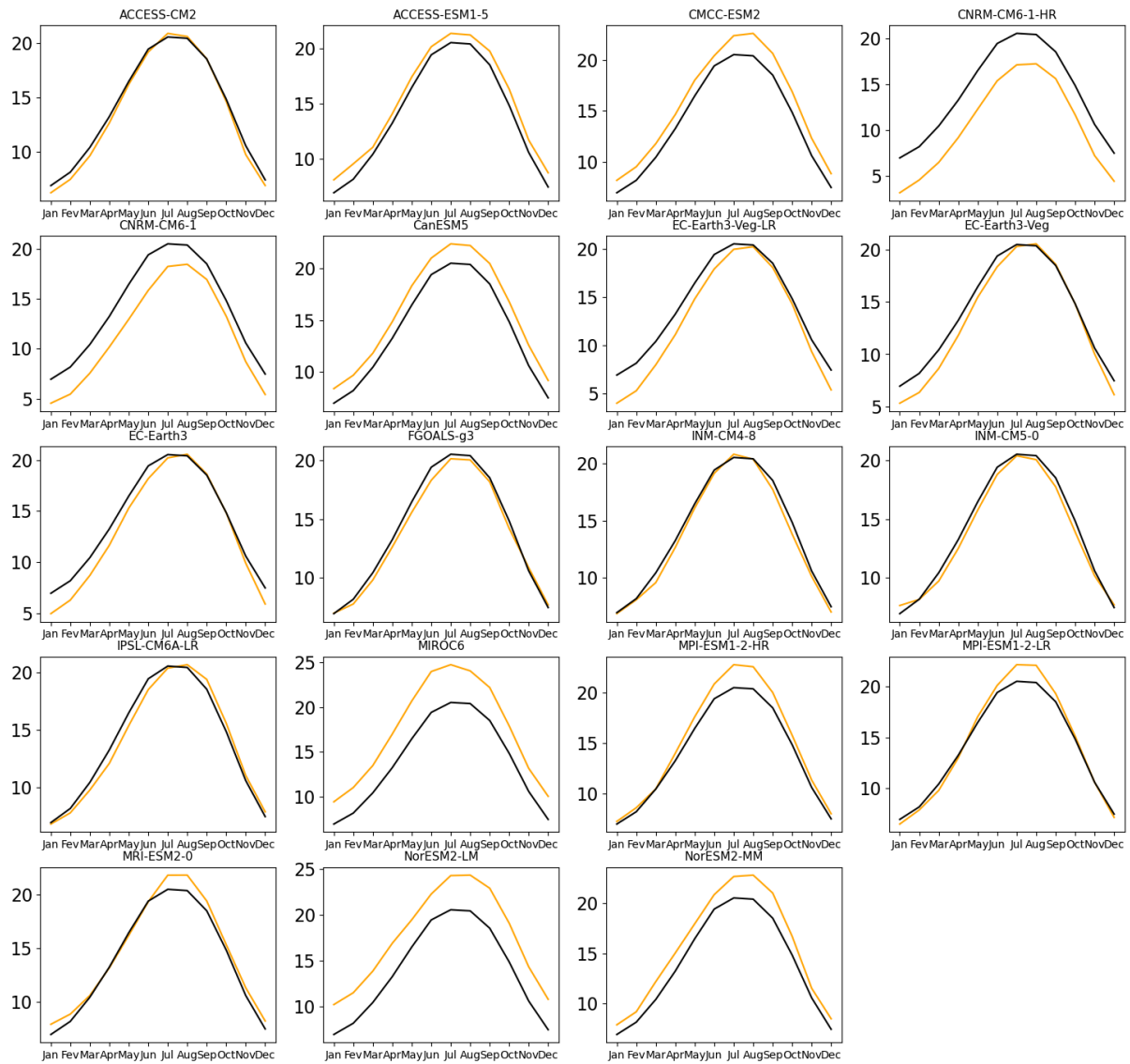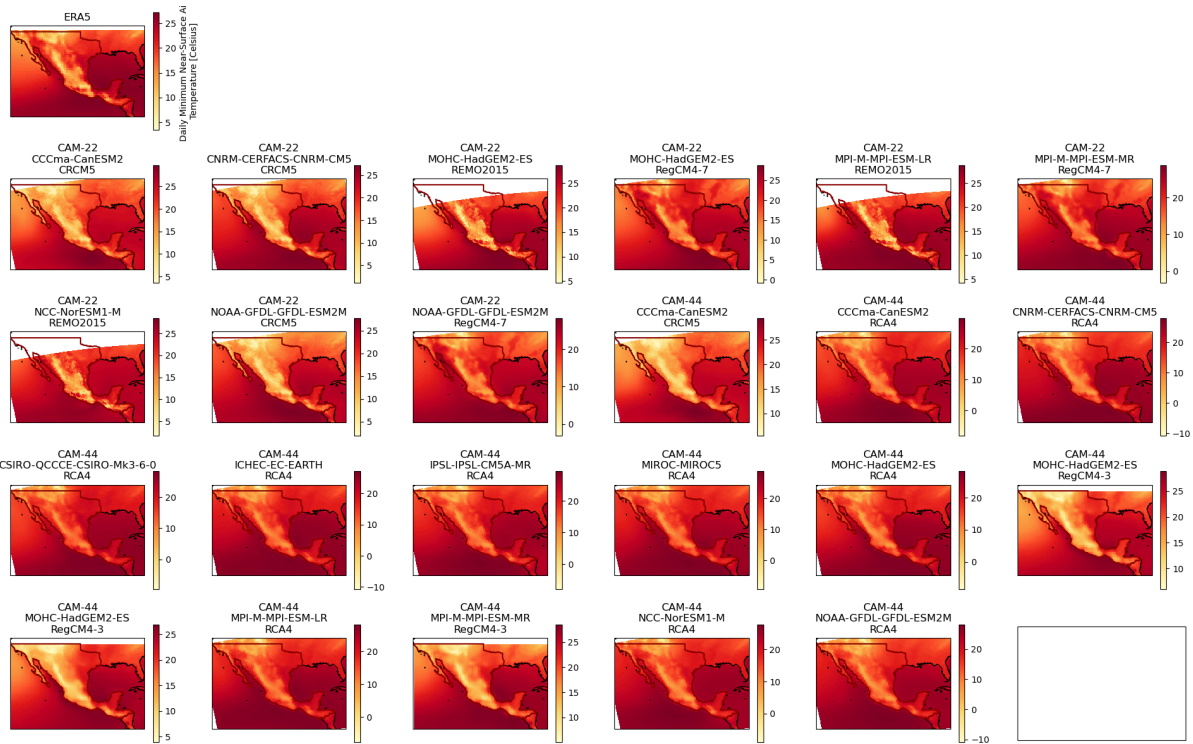

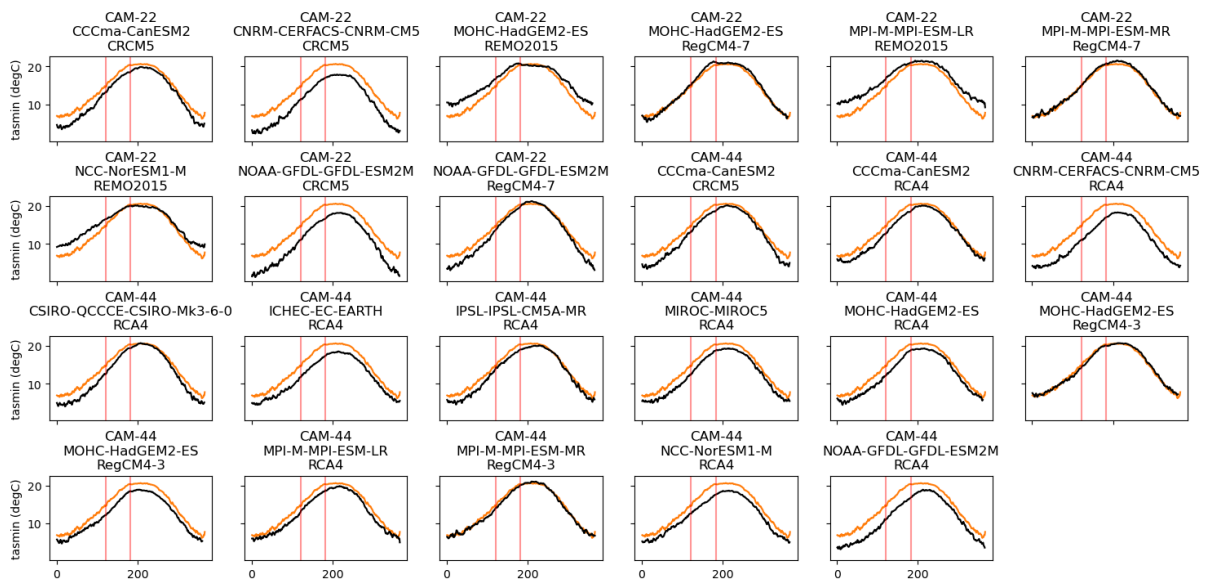*Figure A3. Same as figure A1 but for CORDEX models*
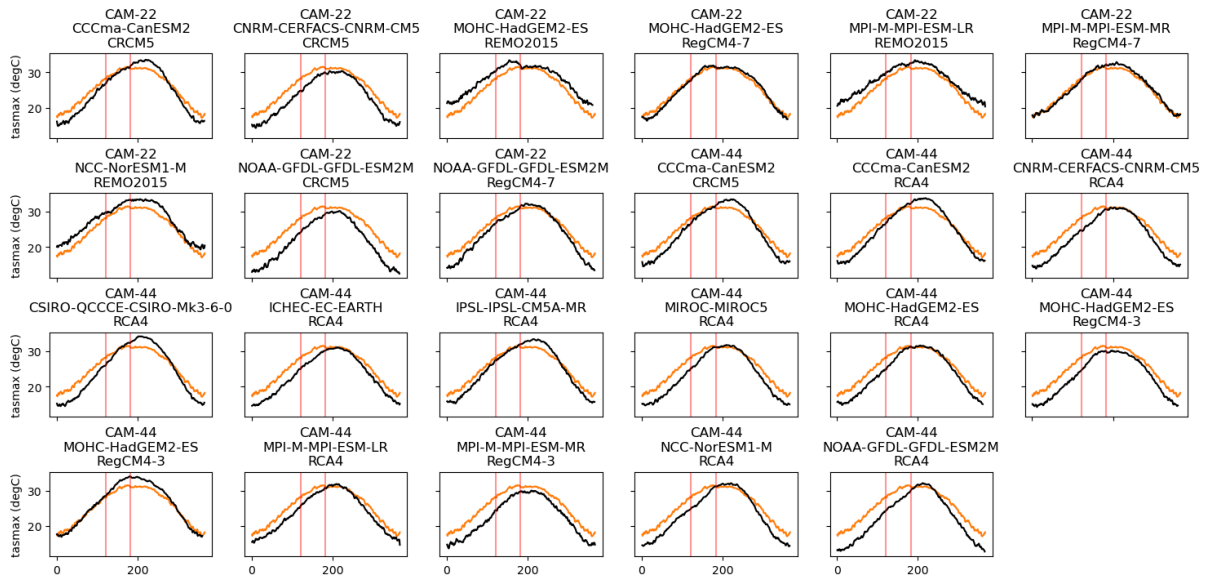
Figure A4. Same as figure A2 but for CORDEX models
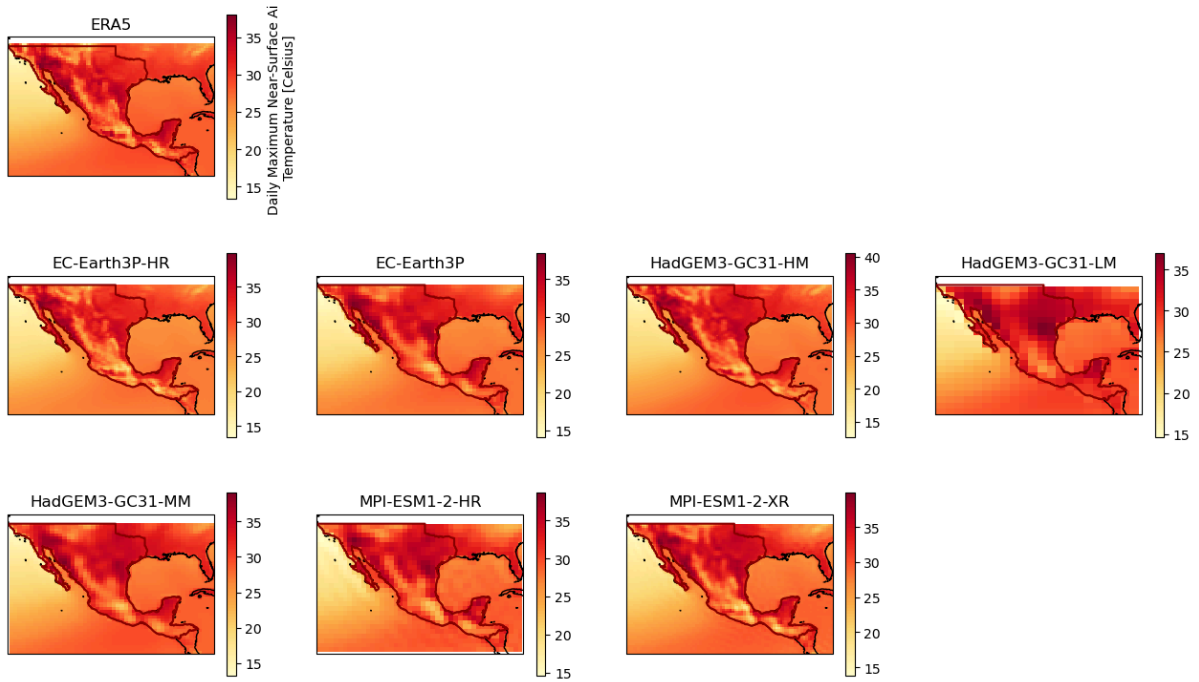
Figure A5. Same as figure A1 but for HiResMIP models
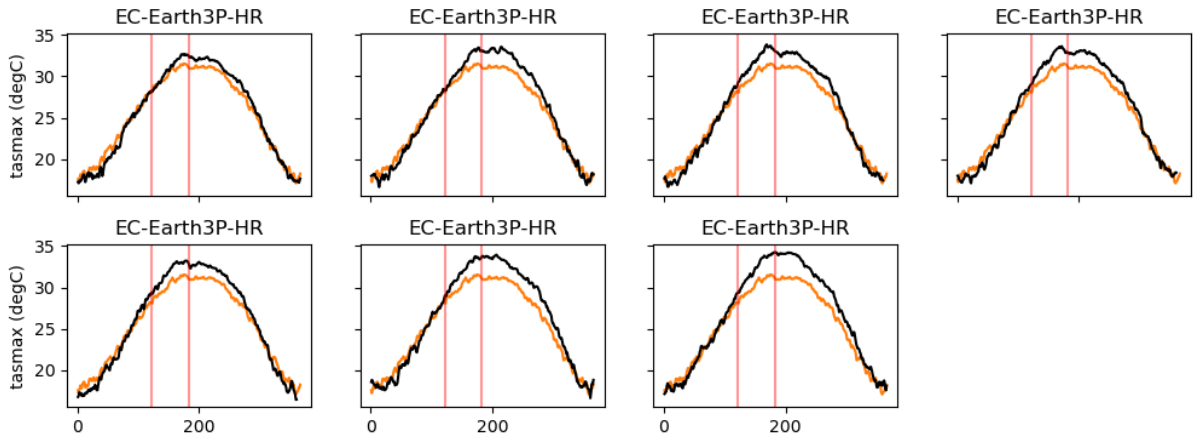
Figure A6. Same as figure A2 but for HiResMIP models

May_June average Tmin 1991-2020

Figure A7. Average minimum temperature for May-June over a climatological period of 1991-2020 of ERA5 and CMIP6 models

Figure A8: Seasonal cycle of maximum temperature over a climatological period of 1991-2020 of ERA5 and CMIP6 models over the study area.

Figure A9. Same as figure A7 but for CORDEX models

Figure A10. Same as figure A8 but for CORDEX models

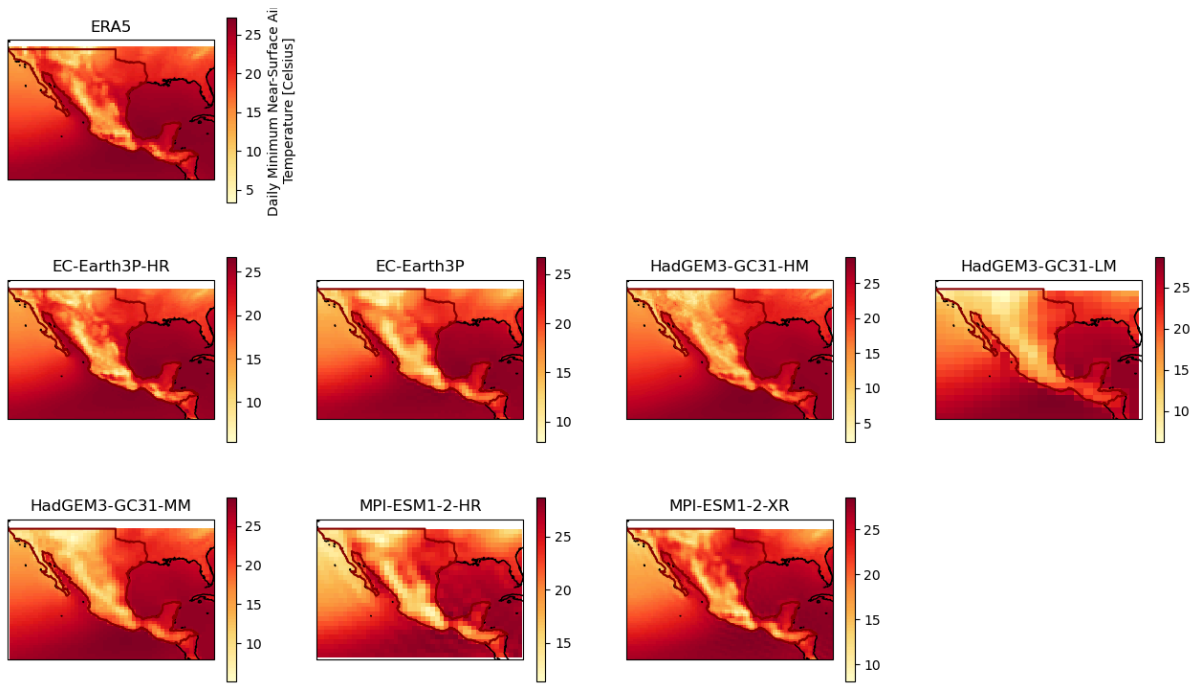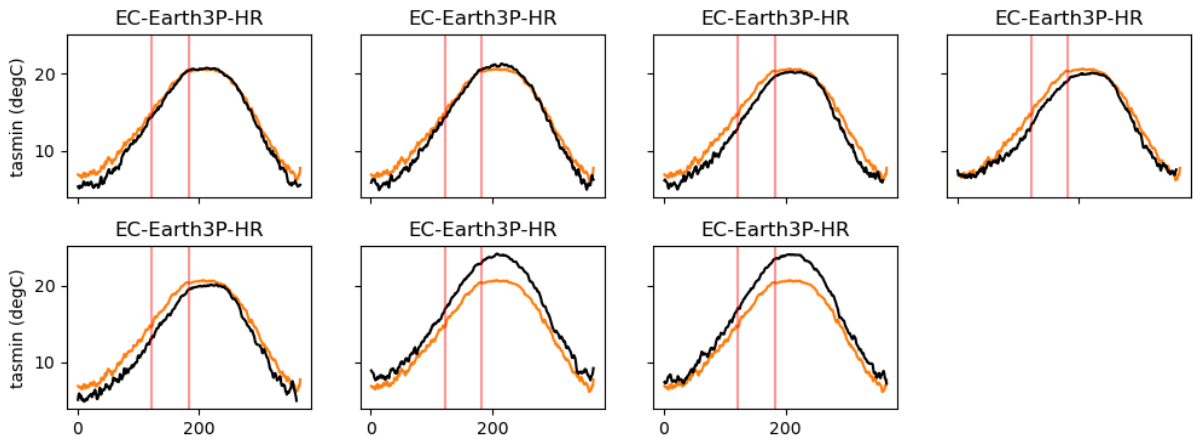*Figure A11. Same as figure A7 but for HiResMIP models*

Figure A12. Same as figure A8 but for HiResMIP models